МІНІСТЕРСТВО ОСВІТИ І НАУКИ УКРАЇНИ
ХАРКІВСЬКИЙ НАЦІОНАЛЬНИЙ УНІВЕРСИТЕТ
імені В. Н. Каразіна

Кафедра неорганічної хімії

До захисту допускаю

_____ Завідувач кафедри

«_16_» _травня____ 2025 р. к.х.н., доц. М. М. Волобуєв

СТРУКТУРНІ ТА ТРАНСПОРТНІ ВЛАСТИВОСТІ РОЗЧИНІВ LiFSI ТА LiFTFSI У ЕТИЛМЕТИЛ КАРБОНАТІ ТА N,N-ДІЕТИЛ-ТРИФТОРОМЕТАНСУЛЬФОНАМІДІ: МД МОДЕЛЮВАННЯ

Кваліфікаційна робота магістра
ІІ курсу хімічного факультету
БОРОВИК АНАСТАСІЇ
ВІТАЛІЇВНИ

Науковий керівник
к.х.н., доцент Я. В. Колесник
Консультант
к.х.н., професор О. М. Калугін

ХАРКІВ 2025

MINISTRY OF EDUCATION AND SCIENCE OF UKRAINE
V. N. KARAZIN KHARKIV NATIONAL UNIVERSITY

Department of Inorganic Chemistry

Admitted to the defense

_____ Head of department

«_16_» __May____ 2025 p. PhD, docent M. M. Volobuyev

STRUCTURE AND TRANSPORT PROPERTIES OF LiFSI AND LiFTFSI SOLUTIONS IN ETHYL METHYL CARBONATE AND N,N-DIETHYL-TRIFLUOROMETHANESULFONAMIDE: MD SIMULATION

Master's thesis
of the 2nd year student
of the school of Chemistry
BOROVYK ANASTASIIA VITALYIVNA

Supervisor
PhD, docent Ya. V. Kolesnyk
Consultant
PhD, professor O. M. Kalugin

KHARKIV 2025

РЕФЕРАТ

Дана кваліфікаційна робота містить: 67 сторінок, 3 розділи, 14 рисунків, 8 таблиць, 6 додатків, 92 літературних джерела.

Об’єктами дослідження є електроліти, що складаються із солей LiFSI і LiFTFSI, та органічних розчинників – етилметил карбонату та N,N-діетил-трифторометансульфонаміду.

Метою даної кваліфікаційної роботи є прогноз структурних та транспортних властивостей електролітних розчинів на основі солей літію для літій-іонних акумуляторів на основі LiFSI, LiFTFSI, EMC та NDF.

У роботі було побудовано модель силового поля досліджуваних іон-молекулярних систем. Методом молекулярно-динамічного (МД) моделювання проведено розрахунок структурних властивостей, використовуючи функції радіального розподілу (ФРР) та поточних координаційних чисел (ПКЧ). За результатами розрахунків встановлено будову першої сольватної оболонки літію. Динамічні властивості розраховано за середньоквадратичним зміщенням. Проведено аналіз залежності рухливості іонів від природи розчинника та температури. Нами було встановлено залежність вільної енергії сольватації літію від складу електролітного розчину.

Ключові слова: ЛІТІЙ-ІОННІ АКУМУЛЯТОРИ, МОЛЕКУЛЯРНО-ДИНАМІЧНЕ МОДЕЛЮВАННЯ, LiFSI, LiFTFSI, EMC, NDF, СТРУКТУРНІ ВЛАСТИВОСТІ, ТРАНСПОРТНІ ВЛАСТИВОСТІ, ЕНЕРГІЯ СОЛЬВАТАЦІЇ, GROMACS, MDNAES.

ABSTRACT

This work consists of 67 pages, 3 chapters, 14 drawings, 8 tables, 6 appendixes, 92 literature sources.

The research objects are electrolytes composed of LiFSI and LiFTFSI salts and organic solvents – ethyl methyl carbonate and N,N-diethyl-trifluoromethanesulfonamide.

The aim of this work is to predict the structure and transport properties of electrolyte solutions for lithium-ion batteries based on LiFSI, LiFTFSI, EMC and NDF.

In this study, a force field model of the investigated ion-molecular systems was developed. Structure properties were calculated using molecular dynamics (MD) simulation, employing radial distribution functions (RDFs) and the running coordination numbers (RCNs). Based on the calculation results, the structure of the first lithium solvation shell was determined. Dynamic properties were evaluated using the mean squared displacement (MSD) method. The dependence of ion mobility on the nature of the solvent and temperature was analyzed. We established the dependence of lithium solvation free energy on the composition of the electrolyte solution.

Keywords: LITHIUM-ION BATTERIES, MOLECULAR DYNAMIC SIMULATIONS, LiFSI, LiFTFSI, EMC, NDF, STRUCTURE PROPERTIES, TRANSPORT PROPERTIES, SOLVATION ENERGY, GROMACS, MDNAES.

TABLE OF CONTENTS

INTRODUCTION

Lithium-ion batteries (LIBs) are one of the key technologies of modern energy, which have found wide application in various industries – from portable electronics to electric transport. Their popularity is due to high specific energy density, long cyclic service life and environmental safety compared to traditional lead-acid or nickel-metal hydride batteries. However, despite significant progress in the development of lithium-ion batteries, there are several problems that hinder their further development. The main ones are limited thermal stability, the risk of dendrite formation on lithium anodes, the high cost of components and insufficient efficiency at extreme temperatures.

One of the most critical elements of a lithium-ion battery is the electrolyte, which ensures the transfer of lithium ions between the anode and cathode during charging and discharging. The properties of the electrolyte directly affect the efficiency of the battery, its energy density, stability and safety. Traditional electrolytes based on liquid organic solvents, although exhibiting high ionic conductivity, have certain drawbacks, such as low thermal stability and susceptibility to degradation at high temperatures.

Therefore, the relevance of our chosen topic lies in improving lithium-ion batteries by researching new salts and solvents for electrolytes that can enhance their efficiency, safety, and stability, contributing to the development of next-generation energy systems with improved performance.

Among the promising areas in this field, systems based on modern lithium salts, such as LiFSI (Lithium bis(fluorosulfonyl)imide) and LiFTFSI (Lithium (Fluorosulfonyl)(trifluoromethanesulfonyl)imide), which demonstrate improved properties compared to traditional $LiPF_6$, attract particular attention. The combination of these salts with organic solvents, such as EMC (Ethyl methyl carbonate) and NDF (N,N-diethyl-trifluoromethanesulfonamide), allows obtaining electrolytes with high ionic conductivity, increased chemical stability, and lower toxicity.

The above components for electrolytes in lithium-ion batteries are not the only ones that are considered for their future production. For example, ethers, esters, nitriles, sulfones and sulfoxides can also be used as solvents. Some of them can increase anodic stability, and others are more fire-extinguishing than current solvents. Therefore, they are often used as

co-solvents with other compounds to improve various properties of lithium-ion batteries. More details about each class of solvents, as well as other popular lithium salts, will be described in the literature review of this work.

Researchers are faced with the task of investigating the properties of a large number of electrolytes, taking into account different salt concentrations, salt:solvent (or solvent mixtures) proportions, temperature, pressure, etc. Therefore, we chose methods of molecular-dynamics (MD) simulations, since experimental research of new electrolytes requires quite a lot of time and large funding.

The aim of this study is to predict the structural and transport properties of LiFSI and LiFTFSI salt solutions in EMC and NDF solvents at various temperatures using molecular dynamics simulations, with a focus on their application in lithium-ion batteries.

To achieve this goal, the following objectives were pursued:

- conduct a literature review on salts and solvents currently used or considered promising for lithium-ion batteries, and describe the methodology of MD simulations for ion-molecular systems, including an overview of commonly used force fields;
- develop and validate force field model for the selected electrolyte systems;
- perform MD simulations of the studied systems to predict their properties at temperatures of 233.15 K, 298.15 K, 353.15 K;
- analyze the structure properties of the systems;
- calculate the translational self-diffusion coefficients and analyze their temperature dependence;
- analyze the solvation energies of the lithium cation depending on the electrolyte composition.

1 LITERATURE REVIEW

1.1 Electrolytes for lithium-ion batteries

The electrolyte in a lithium-ion battery plays a critical role, as it provides the transfer of ions between the electrodes, which is the basis for the charging and discharging processes [1]. To ensure efficient and safe operation of lithium-ion batteries (LIBs), the electrolyte must meet a few requirements [2-4]:

a) Chemical stability – the electrolyte must remain chemically inert during battery operation. This applies to both internal processes in the cell, including interaction with the electrodes, and external processes related to contact with current collecting elements or packaging materials.

b) Electrochemical stability – the electrolyte must operate in a wide range of potentials without undergoing oxidation or reduction reactions.

c) Thermostability – the electrolyte must have a wide range of liquidus temperatures, i.e. its melting and boiling points must be outside the operating temperature range of the battery.

d) Ionic conductivity – is a key characteristic of an electrolyte, as it determines the ability of ions to effectively participate in the electrochemical reactions that ensure the functioning of the cell.

e) Environmental safety and low toxicity – electrolyte materials must meet modern environmental standards and not pose a threat to health.

f) Affordability – both raw materials and electrolyte production processes should be as cheap as possible.

The properties of lithium-ion battery electrolytes are formed mainly by the choice of salts and solvents, and it is the solvents that largely determine the efficiency of ion transfer [5]. To achieve optimal performance, solvents must meet the following criteria [1, 6]:

a) High polarity and dielectric constant – the dielectric constant (ε) must exceed 15 to ensure efficient salt dissociation and minimize ion pairing.

b) Low viscosity – this is necessary to improve the mobility of ions and, accordingly, increase the electrical conductivity of the electrolyte.

c) Electrochemical stability – solvents must remain chemically inert to the anode surfaces or promote the formation of stable passivation films that improve battery performance.

d) Wide temperature range – solvents should be characterized by low melting point and high boiling point, which allows them to work in different conditions.

e) Safety and cost-effectiveness – materials must be non-toxic, safe to use, and low in cost.

Thus, the electrolyte is the key component that determines the functionality and durability of a lithium-ion battery, and its optimal properties depend on the careful selection of salts and solvents [7, 8].

1.1.1 Lithium salts

As described above, one of the components of any electrolyte for LIBs is a lithium salt, which in one way or another affects the final properties of the battery. The main properties that should be paid attention to when choosing salt, and which, unfortunately, significantly reduce the number of suitable candidates, include [9, 10]:

a) High ionic conductivity. The anion of the lithium salt significantly affects conductivity by altering Li^+ solvation and ionic interactions, depending on the anion's structure and coordination strength.

b) High solubility in the solvents used is necessary to create an electrolyte with a sufficient number of charge carriers.

c) High electrical stability to reduction and oxidation – establishing the boundaries of the so-called electrochemical «window».

d) SEI (Solid Electrolyte Interphase) formatting ability. It forms between the electrode and electrolyte due to reactions between the electrolyte and electrode material. Ideally, only a few materials react, creating an SEI layer that prevents further reactions and allows easy Li^+ ion transport, minimizing resistance. The lithium salt in the electrolyte, whether as a primary salt or additive, greatly influences the SEI's composition, properties, and stability.

$LiPF_6$ (lithium hexafluorophosphate) remains the main salt for commercial electrolytes due to the balance of its properties [11]. Its high solubility in carbonate solvent

mixtures allows the creation of electrolytes with high ionic conductivity. An important factor is its ability to form a stable SEI layer on the surface of the graphite anode, which prevents side reactions and lithium loss. However, $LiPF_6$ has significant disadvantages. At temperatures above 60 °C, it is prone to thermal degradation to form PF_5, a highly reactive component that catalyzes side reactions. The presence of moisture causes the formation of HF acid, which corrodes cathodes and anodes [12]. This limits the use of $LiPF_6$ in high-temperature environments and forces manufacturers to add stabilizers to the electrolytes [13-15].

LiFSI (lithium bis(fluorosulfonyl)imide) is considered one of the most promising alternatives to $LiPF_6$. Its chemical structure provides high thermal stability, making it suitable for high-temperature applications [16]. In addition, LiFSI has a significantly lower hygroscopicity compared to $LiPF_6$, which reduces the risk of electrolyte degradation in humid conditions [17, 18].

Experimental studies have demonstrated that LiFSI-based electrolytes have ionic conductivity equal to or higher than that of $LiPF_6$. For example, in the work of Chidiac et al. [19] it was shown that LiFSI in combination with solvents such as ethylene carbonate (EC) and dimethyl carbonate (DMC) provides stable cycling of batteries even at high current loads [20].

Despite its advantages, LiFSI has the disadvantage of increased corrosion of the aluminum cathode current collectors [21]. This limits its use in its pure form, but the combination of LiFSI with other salts (e.g. $LiPF_6$) allows to minimize this effect [19, 22].

$LiBF_4$ (lithium tetrafluoroborate) is another interesting salt for lithium-ion batteries. Its key advantages include high thermal stability and moisture resistance. Unlike $LiPF_6$, $LiBF_4$ does not degrade in contact with water and does not form HF acid. However, $LiBF_4$ has a lower ionic conductivity, which limits its use in electrolytes for high-performance systems. It is often used as an additional salt to improve SEI stability or in electrolytes for specialized batteries where stability is more important than conductivity [14].

The research also examines less common salts such as lithium perchlorate ($LiClO_4$) and lithium nitrate ($LiNO_3$). $LiClO_4$ exhibits high ionic conductivity and stability, but its use is limited by the risk of explosion. $LiNO_3$ is used primarily in lithium-sulfur batteries as an additive to stabilize electrode surfaces [23].

$LiAsF_6$ (lithium hexafluoroarsenate), although less common, is still used in certain types of lithium-ion batteries. It has a high resistance to thermal decomposition and has high electrical conductivity, making electrolytes useful for high-power batteries. However, due to the toxicity and hazard of the arsenic compound, its use is limited, and this salt is often chosen only in situations where other options are not suitable [7, 8].

Table 1.1 presents the main physicochemical properties of the most commonly used lithium salts in lithium-ion batteries [17, 24].

Table 1.1 Chemical structures, melting temperatures (T_m), ionic conductivities at 25 °C (σ) and viscosities at 25 °C (η) of the most commonly used salts in lithium-ion batteries

Salt	Chemical structure	T_m, °C	σ, mS cm^{-1}	η, cP
$LiClO_4$	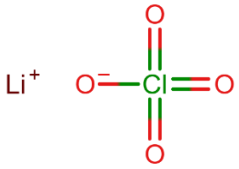	236	5.6[a] 6.3[b]	2.77[b]
$LiBF_4$	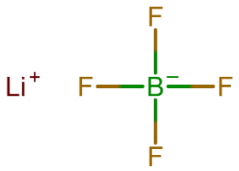	293	3.4[a] 3.7[b]	2.23[b]
$LiPF_6$	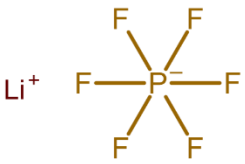	200	5.8[a] 9.3[b]	3.00[b]
LiTf	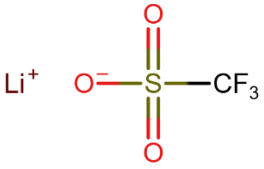	>300	1.7[a]	-
LiTFSI	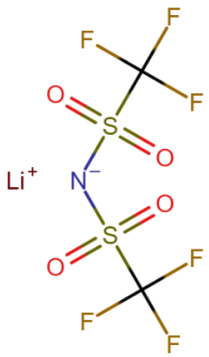	234	5.1[a] 7.6[b]	3.40[b]

LiFSI	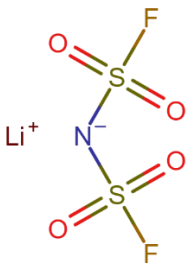	130	9.7[b]	2.96[b]

[a] 1 M LiX in PC at 25 °C
[b] 1 M LiX in EC/EMC (3:7, v/v) at 25 °C

1.1.2 Organic solvents

Organic solvents play an important role in providing a medium for dissolving lithium salts and transporting ions in lithium-ion batteries. The most commonly used solvents are ethylene carbonate (EC), dimethyl carbonate (DMC), diethyl carbonate (DEC), and propylene carbonate (PC). The choice of solvents is based on their physicochemical properties, such as dielectric constant, viscosity, and thermal stability [25].

Esters are used because of their resistance to oxidation at anodes. However, they have limitations in operation at low potentials, which is overcome by the formation of a protective SEI layer that stabilizes the surfaces of cathodes and anodes. The most popular esters in lithium-ion batteries are dimethyl carbonate DMC (acyclic), ethylene carbonate EC and propylene carbonate PC (cyclic) [26].

To improve the characteristics of esters, the carbon chains are modified, forming compounds with different degrees of branching (e.g., n-BMC, i-DMC, s-BMC, DC, PIC). Although they have higher viscosity and lower ionic conductivity, this is compensated by increased capacity after several charge cycles. It was found that this effect is stronger when the branching point is closer to the carbonyl group [9].

For operation at low temperatures, fluorinated acyclic carbonates are synthesized. Their mixtures with EC, DMC and DEC demonstrate increased performance and better SEI formation [27].

Nitriles, namely acetonitrile (AN), are a common solvent for lithium-ion batteries. Its advantages include low viscosity and high dielectric constant, which provides good ionic conductivity. Its disadvantage is a narrow window of electrochemical stability. For LIBs alkoxy-substituted nitriles (3-methoxypropionitrile (MPN), 3-ethoxypropionitrile (EPN), (2,2,2-trifluoro)ethoxypropionitrile (FEPN)) have been developed to improve performance based on $Li_4Ti_5O_{12}$, as well as dinitriles (malonitrile (MAN), succinonitrile (SCN),

glutaronitrile (GLN), adiponitrile (AND) et.) to improve resistance to oxidation and thermal degradation. Nitriles demonstrate anodic activity, but their cyclic stability still needs to be improved [28, 29].

Sulfones and sulfoxides have high dielectric constants, low flammability, and stability at high anode voltages. Their main disadvantages are poor electrode wettability, poor ionic conductivity, and inability to form SEI on graphite anodes. Ethyl methyl sulfone (EMS), tetramethylene sulfone (TMS), and other derivatives (FS, BS, EVS) are characterized by high anodic stability. New compounds such as ethyl isopropyl sulfone (EiPS) and ethyl isobutyl sulfone (EiBS) have a wide range of liquid states, dissolve tetraalkyl ammonium salts well, and exhibit improved ionic conductivity. To reduce viscosity and melting point, synthetic addition of oligoether linkages of various lengths to sulfone is being investigated [30-32].

Phosphorus-containing solvents such as phosphonates, phosphazenes, and phosphates are used to reduce flammability and increase anodic stability. For example, dimethyl methylphosphonate (DMMP) was initially considered a flame retardant component but was later recognized as an effective additive for high-voltage cathodes [33].

Siloxane and silane compounds have low dielectric constants. To increase their conductivity, siloxanes with oligoether chains of various lengths capable of dissociating lithium salts have been synthesized. Also, some trimethylsilane derivatives have achieved conductivity of 1 mS cm^{-1} [34].

Organic esters have rarely been used in lithium-ion batteries due to their instability at 4 V cathodes. However, fluorinated esters such as F-EPE, in combination with fluorinated carbonates, provide stable operation of high-voltage cathodes such as $LiNi_{0.5}Mn_{1.5}O_4$, even at elevated temperatures [35].

Table 1.2 shows the main physicochemical properties of the most commonly used solvents in lithium-ion batteries [17, 24, 36].

Table 1.2 Chemical structures, melting temperatures (T_m), boiling temperatures (T_b), flash temperatures (T_f), viscosities at 25 °C (η) and dielectric constants at 25 °C (ε) of the most commonly used solvents in lithium-ion batteries

Solvent	**T_m, °C**	**T_b, °C**	**T_f, °C**	**η, cP**	**ε**

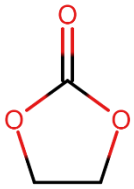 Ethylene carbonate **(EC)**	36.4	248	160	1.9 (40 °C)	89.78

Table 1.2 Continued

Solvent	**T_m, °C**	**T_b, °C**	**T_f, °C**	**η, cP**	**ε**
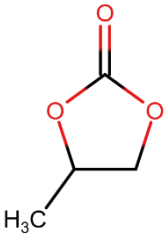 Propylene carbonate **(PC)**	-48.8	242	132	2.53	64.92
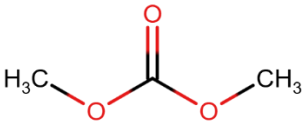 Dimethyl carbonate **(DMC)**	4.6	91	18	0.59	3.107
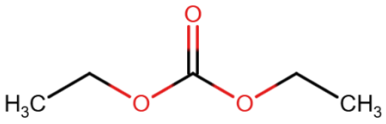 Diethyl carbonate **(DEC)**	-74.3	126	31	0.75	2.805
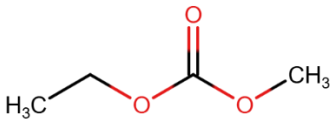 Ethyl methyl carbonate **(EMC)**	-53	110	-	0.65	2.958
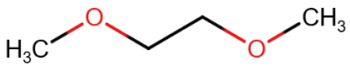 Dimethoxyethane	-58	84	0	0.46	7.18

(DME)					
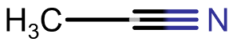 Acetonitrile **(AN)**	-43.8	81.6	-	0.37	36.6
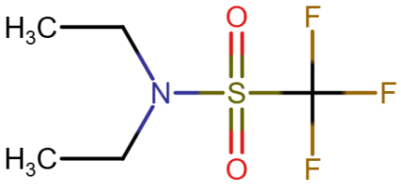 N,N-diethyl-trifluoromethanesulfonamide **(NDF)**	-43.0	-	-	1.57	20.42

1.2 Molecular-dynamics simulations of ion-molecular systems

In recent years, molecular dynamics (MD) simulations have gained significant popularity among researchers due to their higher efficiency and lower cost compared to traditional laboratory-based experiments [37]. The application scope of MD simulations is broad and interdisciplinary, spanning fields such as biochemistry [38, 39], materials science [40], and chemical physics [41, 42]. A particularly prominent area of research involves the development and study of pharmaceutical compounds through molecular design techniques [43].

Special attention and scientific interest has arisen around the development of new electrolytes for energy storage devices (such as batteries, supercapacitors, etc.) [44]. MD simulations serve as a powerful tool for predicting the structural and transport properties of alternative electrolytic systems [45]. They enable to study the influence of temperature, salt concentration, nature of the solvent on density, viscosity, electrical conductivity, electrochemical stability window (ESW), SEI formation and other characteristics that are significant in the use of a particular electrolyte [46].

The foundation of molecular dynamics (MD) simulations lies in the numerical integration of Newton's equations of motion for all particles within the system under investigation. These equations are solved using a small time step simultaneously for all atoms. Each particle is defined by its position and velocity in phase space, and the collective evolution of these variables forms the system's trajectory [38, 47].

The first stage of MD simulation involves constructing the force field of the system – i.e., defining the parameters that describe both short-range (Van der Waals) and long-range

(electrostatic) potentials (equation for the potential energy of the system is given in Section 2 of this work). This step is critical because the accuracy of the force field directly affects the reliability of the predicted system properties [48].

To determine the size of the system, a basic cell is defined, which is a part of space with real or imaginary boundaries and is characterized by shape, size, number of particles with initial coordinates and velocities. This box is then replicated in space using periodic boundary conditions (PBCs), which eliminate edge effects and allow the system to be treated as if it were infinite in extent [49, 50].

The second stage involves system initialization and equilibration, during which the system is brought to thermodynamic equilibrium. The duration of the equilibration phase depends on system size and may range from hundreds of picoseconds to several tens of nanoseconds. Before integration begins, initial atomic positions are assigned either from experimental data or generated randomly, and particle velocities are typically drawn from a Maxwell-Boltzmann distribution corresponding to the desired temperature [51].

The simulation is performed under a specified thermodynamic ensemble, which defines which macroscopic properties of the system are held constant: energy (E), volume (V), temperature (T), or pressure (P). Common ensembles include *NVE* (microcanonical), *NVT* (canonical), and *NPT* (isobaric-isothermal) [38].

Thermostats are used to maintain constant temperature throughout the simulation. Common examples include the Berendsen, Nose-Hoover, Velocity-rescaling thermostats. In *NPT* ensembles, a barostat, such as the Berendsen or Parrinello-Rahman barostat, is also employed to control pressure by adjusting the simulation box volume [52].

As noted earlier, the system trajectory is generated by integrating Newton’s equations of motion over time. The equations of motion are integrated using dedicated numerical algorithms such as the Verlet, or leap-frog integrators for monoatomic liquids, or SHAKE (RATTLE), FIQA or NOSQUISH algorithms for multiatomic molecules [47, 53].

Once equilibrium is achieved, a production run is carried out, during which structural, dynamic, or energetic properties of the system are computed. These properties are obtained by statistical averaging of relevant microscopic variables over the generated trajectory [54, 55].

In article Da Silva D. et al. [56], aqueous solutions of sodium perchlorate of varying concentrations were investigated to encompass both «salt-in-water» and «water-in-salt»

systems. The choice of this research subject is justified by the potential application of such systems in sodium-ion batteries or supercapacitors, which are seen as promising alternatives to lithium-based technologies. The primary aim was to study five systems with different salt concentrations in water using molecular dynamics simulations. Specifically, the study involved the calculation of density as a function of molar concentration, analysis of structural properties (via radial distribution functions), and transport properties (viscosity calculated using the Green-Kubo formula and diffusion coefficients determined by the mean squared displacement method).

The study revealed that with increasing electrolyte concentration, the coordination number of Na^+ and ClO_4^- ions with water molecules decreases, indicating the formation of ionic aggregates and reduced ion hydration.

The viscosity of the electrolytes increases nearly linearly with concentration, while ionic conductivity reaches a maximum at 5 mol dm^{-3} and then declines with further concentration increase. This behavior is attributed to the reduced ion mobility caused by ion pair formation and a decrease in the number of free water molecules. The diffusion coefficients decrease as the salt concentration increases. Water molecules exhibit the highest diffusion coefficients, whereas sodium cations exhibit the lowest. Notably, the anion's mobility is significantly affected by salt concentration – at the highest concentration, the mobility of the anion is the lowest.

Thus, the study demonstrates that selecting the optimal electrolyte concentration is key to achieve a balance between stability, conductivity, and energy efficiency in supercapacitors.

Zhang Y. et al. [57] investigated a water-in-salt system of a promising electrolyte LiTFSI, due to its high ionic conductivity, for use in lithium-ion batteries. In particular, the study focused on the structure of the aqueous electrolyte.

The results showed that at high salt concentrations, water molecules form ordered structures or clusters, which contribute to enhanced ionic conductivity. It was found that water molecules surrounding lithium ions form long-lived interaction structures, where the ionic environment is more ordered compared to less concentrated systems.

Shao Y. et al. [58] studied the temperature dependence of ionic conductivity in concentrated electrolyte solutions. The study focused on prototypes of alkaline electrolytes – aqueous NaOH solutions, selected due to the hydroxide ion's exceptionally high

electrochemical activity. The study employed reactive MD simulations to investigate proton transport processes as a function of temperature across solutions of varying concentrations.

The results showed that increasing the temperature to 323 K enhances the ionic conductivity in concentrated NaOH solutions. This effect is attributed to the intensification of the proton transport mechanism (the Grotthuss mechanism) and a decrease in solution viscosity.

The study Tan W. et al. [59] focused on systems with a solid polymer electrolyte PEC, with LiTFSI salt concentrations ranging from 5 to 120 mol%. Particular attention was given to analyzing the behavior of individual Li^+ ions, which were classified as either «fast» or «slow» based on their mean squared displacement.

The results revealed that «fast» Li^+ ions exhibit conductivity approximately ten times higher than that of «slow» ions and, despite their reduced number at high salt concentrations, they account for nearly 70 % of the total charge transport.

Additionally, the solvation free energy was calculated, showing that «fast» Li^+ ions possess higher solvation free energy, indicating weaker solvation and greater mobility. At salt concentrations exceeding 80 mol%, ionic aggregates form, limiting the coordination capabilities of both PEC and $TFSI^-$.

In the article Sampaio A. et al. [60] investigate two ionic liquids (ILs) with the same anion but different cations – sulfonium and phosphonium. The study demonstrates that the choice of cation in ILs significantly affects the performance of supercapacitors. Sulfonium-based ILs can provide higher energy density and faster charging without a significant increase in viscosity or reduction in conductivity.

Bedrov D. et al. [61] published a review article dedicated to the application of polarizable force fields in molecular dynamics (MD) simulations of ionic liquids and other electrolytes for studying structural and transport properties. The authors compared the most widely used force fields and presented the resulting diffusion coefficients, viscosities, and ionic conductivities obtained for each model.

2 SIMULATION METHODOLOGY

2.1 Research objects

For MD simulation salts LiFSI and LiFTFSI were chosen in a mixture with solvents EMC and NDF. The choice of these salts is explained by the fact that there is currently little research by MD simulation method on their use in lithium-ion batteries. However, they are expected to have good prospects due to their high stability at high temperatures [19]. If we talk about solvents, EMC is quite popular and therefore the study of its mixture with the above-mentioned salts is of strong scientific interest. It has been previously studied that NDF can be used to improve the safety of lithium-ion batteries, so in addition it is important for us to evaluate its other important properties [36].

The structure of the EMC, NDF, FSI^- and $FTFSI^-$ are shown at Figure 2.1.

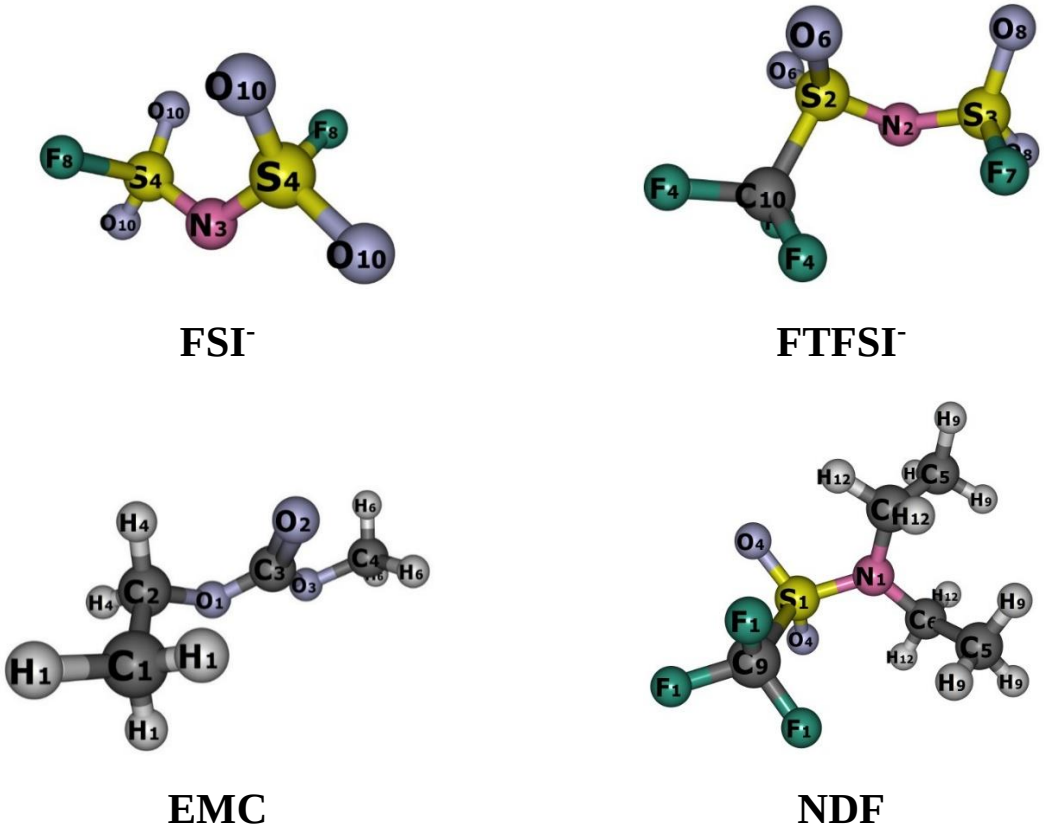

Figure 2.1 Structure of the FSI^- and $FTFSI^-$ anions and molecular solvents of EMC and NDF.

To calculate the number of particles for the MD simulation we used the molar ratio. Systems with different numbers of particles are presented in Table 2.1. The total numbers of

particles are different because it was important for us to keep their exact ratio within the system.

Table 2.1 The composition of the simulated systems.

	Number of molecules				∑	Molar ratio
	Salt		Solvent			
	LiFSI	**LiFTFSI**	**EMC**	**NDF**		
1. LiFSI-EMC	94	-	909	-	1003	1:9.67
2. LiFSI-NDF	125	-	-	880	1005	1:7.04
3. LiFTFSI-EMC	-	94	909	-	1003	1:9.67
4. LiFTFSI-NDF	-	125	-	880	1005	1:7.04

2.2 Force fields

Force fields (FFs) are key components of molecular dynamics (MD) simulations, determining the potential energy of a system and, consequently, the forces acting on the particles. For ion-molecular systems, the following types of force fields are used: non-polarizable, polarizable and reactive [40].

Classical (or non-polarizable) force fields use fixed parameters to describe interatomic interactions without taking into account changes in electronic polarization. Non-polarizable FFs such as OPLS, AMBER and GROMOS, originally developed in the 1980s – 1990s, remain widely utilized in molecular simulations. They are continuously improved and parameterized to suit the specific physicochemical properties of interest [62].

Force fields based on the OPLS model are commonly employed for the simulation of ionic liquids. The parameterization is motivated by the limited investigation of the force field model's ability to reproduce the structural properties of the solvent, due to the insufficient availability of experimental data. In the study by K. Yue et al. [63], the force field was refined through the development of charge-scaled OPLS-VSIL, which introduces a virtual site to redistribute negative charge into the ring plane of imidazole, thereby improving the modeling of hydrogen bonding.

Currently, the most advanced version of the force field is OPLS/2020. It represents a refinement of the earlier all-atom OPLS-AA model, which demonstrated limitations in accurately reproducing the dynamic properties of molecular systems. OPLS/2020 is applied

in the simulation of liquid alkanes with complex branched structures, as well as alcohols, ethers, and biomolecules [64].

Automated force field parameter generation tools have become increasingly popular in molecular simulations. Among them, the LigParGen web service is widely used for generating nonbond parameters, bond lengths, angles, and dihedrals consistent with the OPLS-AA force field. This service was utilized in the experimental part of the present thesis. LigParGen is frequently applied to parameterize a broad range of organic molecules and electrolytes. In the study Yadav et al. [65] performed a comparative analysis of LigParGen and other parameterization services (SwissParam and CGenFF, based on generating CHARMM force fields) for drug-like compounds, reporting a strong agreement with experimental data. However, they also highlighted substantial differences in parameters across platforms, which should be carefully considered when selecting a tool for specific simulation objectives.

The AMBER force field, particularly in its refined forms, is widely utilized in molecular dynamics simulations of biomolecules. Parameterization may be carried out either partially (for example, by adjusting torsional angles to improve the accuracy of structural features) or comprehensively, through complete reparameterization using quantum mechanical calculations. For smaller systems, such as organic solvents or ionic liquids, a General AMBER Force Field (GAFF) is used [66-68].

Unlike the previously discussed force fields, GROMOS is not an all-atom model but a united-atom model, primarily applied to the simulation of large systems such as biomolecules. Ongoing research efforts are focused on improving the GROMOS force field by developing a new code architecture to enable the implementation of advanced functionalities [69]. Additionally, comparisons between different versions of the GROMOS force field family are actively conducted to identify the most suitable parameterization for specific molecular systems [70, 71].

Among the force fields discussed above, OPLS appears to be the most suitable for molecular dynamics simulations of ion-molecular systems, as supported by comparative studies evaluating different models for such systems [62, 72].

Studies have demonstrated that for systems where electrostatic interactions play a critical role, the use of polarizable force fields is generally preferable. Among the most widely used is the CHARMM force field [73, 74]. For ionic solutions, the CHARMM

Drude model is commonly used, which employs the Drude oscillator approach [75]. Polarizable force fields are essential for accurate modeling of ionic liquids and electrolytes, particularly under conditions of high ionic concentration and in the vicinity of charged surfaces. Their application enables improved reproduction of experimental data and facilitates a deeper understanding of the underlying mechanisms governing the behavior of such systems [61].

Reactive force fields offer a deeper understanding of atomistic processes by enabling the explicit modeling of bond breaking and formation [76].

In the context of lithium-ion battery research, these models are extensively employed to simulate the behavior of anode materials during charge-discharge cycles [77], investigate the formation of the solid electrolyte interphase (SEI) on electrode surfaces [78], and to model interfacial chemical reactions between the electrode and electrolyte that critically influence SEI composition and stability [79].

Recently, the integration of machine learning techniques with reactive force fields has gained significant momentum. For instance, hybrid models combining reactive force fields with neural networks (ReaxFF-MPNN) have been developed to more efficiently compute bond orders and energies [80]. A particularly impactful advancement involves the application of machine learning to study lithium diffusion and other transport properties within cathode materials. Neural networks were trained to perform *ab initio* simulations, producing results that closely align with experimental observations. This research is especially important, as it allows *ab initio* modeling of complex and large-scale systems that were previously computationally intractable [81].

In our work we have created two systems of charges for each electrolyte. The coordinates of atoms, charges, sigma and epsilon parameters for solvents and anions for first system were generated in LigParGen Server [82]. For anions charges were recalculated excluding Hydrogen atoms using Gaussian16 software (B3Lyp functional, 6-31G(d,p) basis) [83]. We have also highlighted symmetric atoms and calculated the arithmetic mean of their charges.

For the second system sigma and epsilon parameters were taken from LigParGen model too, but we have completely recalculated charges using Gaussian16 (M062X functional, AUG-cc-PVTZ basis, CHelpG charge calculation scheme) and took average values for symmetrical atoms.

For the Li^+ the potential model has been used from OPLS-AA [84].

In this work, short-range (Van der Waals) potentials are described by the Lennard-Jones potential (equation 2.1).

$$U^{LJ}\left(r_{ij}\right)=4\varepsilon_{ij}\left[\left(\frac{\sigma_{ij}}{r_{ij}}\right)^{12}-\left(\frac{\sigma_{ij}}{r_{ij}}\right)^{6}\right] \tag{2.1}$$

The Coulomb interaction equation describes long-range electrostatic potentials (equation 2.2).

$$U^{Coul}\left(r_{ij}\right)=\frac{q_i q_j e^2}{4\pi\varepsilon_0 r_{ij}} \tag{2.2}$$

In general, the total potential energy is expressed as a sum of terms and is represented in equation 2.3. The first four terms are the contributions of intramolecular interactions – stretching of bonds, bending of angle, dihedral and improper torsions. And the last terms describe nonbonded interactions.

$$U_{tot}=\sum_{ij}^{bonds}\frac{k_{r,ij}}{2}\left(r_{ij}-r_{0,ij}\right)^2+\sum_{ijk}^{angles}\frac{k_{\theta,ijk}}{2}\left(\theta_{ijk}-\theta_{0,ijk}\right)^2+\sum_{ijkl}^{dihedral}\sum_{n=0}^{5}C_n\left(\cos\left(\psi_{ijkl}\right)\right)^n+$$

$$+\sum_{ijkl}^{improper}k_{\phi,ijkl}\left(1+\cos\left(n\phi_{ijkl}-\phi_{s,ijkl}\right)\right)+\sum_{ij}^{nonbonded}\left(4\varepsilon_{ij}\left[\left(\frac{\sigma_{ij}}{r_{ij}}\right)^{12}-\left(\frac{\sigma_{ij}}{r_{ij}}\right)^{6}\right]+\frac{q_i q_j}{4\pi\varepsilon_0 r_{ij}}\right), \tag{2.3}$$

The charge distribution, q, Lennard-Jones parameters, σ and ε, intramolecular parameters, force constants k_i for EMC and NDF are presented in Appendix A, for FSI^- and $FTFSI^-$ anions – in Appendix B. An example of an itp-file containing the atomic masses, the sigma and epsilon parameters used for molecular dynamics simulations in GROMACS is provided in Appendix C.

2.3 Details of molecular-dynamics simulations

The generation of cubic cells was carried out in the MDNAES software [85].

All simulations have been carried out using GROMACS software [86]. We performed calculations in *NPT* ensemble (for equilibration) and *NVT* ensemble (for calculating structure and dynamic properties) at three different temperatures – 233.15 K, 298.15 K and 353.15 K, which was kept constant by velocity-rescaling thermostat (τ_T = 1 ps). The pressure 1 bar was kept constant by Parrinello-Rahman barostat (τ_p = 50 ps). The

leap-frog algorithm is the basis of the integration of motion equations. Time step of all simulations was equal to 0.5 fs.

The equilibration, calculation of density and structure properties have been performed for 5 ns for each simulation.

Figure 2.2 shows an example of the system reaching thermodynamic equilibrium. It was found that for all studied objects, 5 nanoseconds are sufficient to achieve equilibrium state.

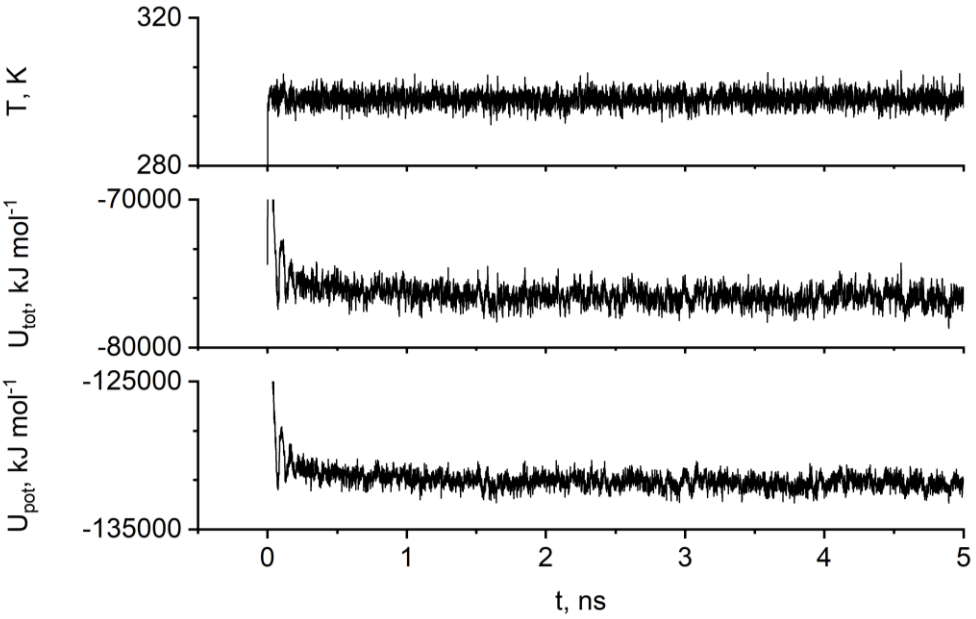

Figure 2.2 The dependence of temperature (top), total energy (middle), and potential energy (bottom) on simulation time as an example of bringing a system into thermodynamic equilibrium.

The calculation of dynamic properties consisted of 5 consecutive simulations with a total duration of 50 ns. For some systems, the simulation time was extended to 250 ns to improve the statistical reliability of the results.

The calculation of the solvation free energy has been performed for 1 ns for each value of the free-energy coupling parameter λ.

2.4 Structure properties calculations

The structure properties of electrolytes were analyzed using radial distribution functions (RDF) and running coordination numbers (RCN).

Due to particle interactions, the position of each particle is influenced by the positions of the surrounding ones. The RDF captures this correlation, reflecting the spatial relationships between particles. As a pair correlation function, it provides insight into how particles are arranged within the studied system. The RDF describes the likelihood of locating a given particle at a specific distance from a reference particle, considering all spatial directions. We can determine the RDF as *g(r)* [87, 88]:

$$g_{ij}(r) = \frac{V}{N_j} \frac{n_{ij}(r)}{4\pi r^2 \Delta r}, \tag{2.4}$$

where V is the volume of the system, N_j is the total number of particles j, n_{ij} represents the average number of particles j in a spherical shell with a thickness Δr at the distance of r from the reference particle.

The first maximum in the RDF indicates the most probable distance at which particles are located around a reference particle, corresponding to the first coordination shell where the nearest neighbors are found. Following this, the first minimum represents the distance beyond the first coordination shell where the particle density decreases to its lowest point, marking the boundary between the first and second coordination shells. The second maximum is the most probable distance between the particle located in the center and the second coordination shell.

If we integrate *g(r)* in spherical coordinates to the distance r we can get RCN, which can be determined as *n(r)* [87, 88]:

$$n_{ij}(r) = \frac{N_j - \delta_{ij}}{V} \int_0^r 4\pi r^2 g_{ij}(r)\, dr \tag{2.5}$$

The RCN illustrates the number of observed particles that can be located within a specific range around the reference particle.

To investigate the coordination of Lithium ions around anions and solvent molecules, we selected their most negatively charged atoms. Figure 2.3 shows chemical structures of the studied ions and molecules, and the green circles indicate the putative coordination centers.

To investigate the coordination of anions around solvent molecules, in the former we chose the most negatively charged atoms, and in the latter – the most positive ones. Figure 2.4 shows the chemical structures of the studied ions and molecules, and the putative coordination centers are marked with red circles.

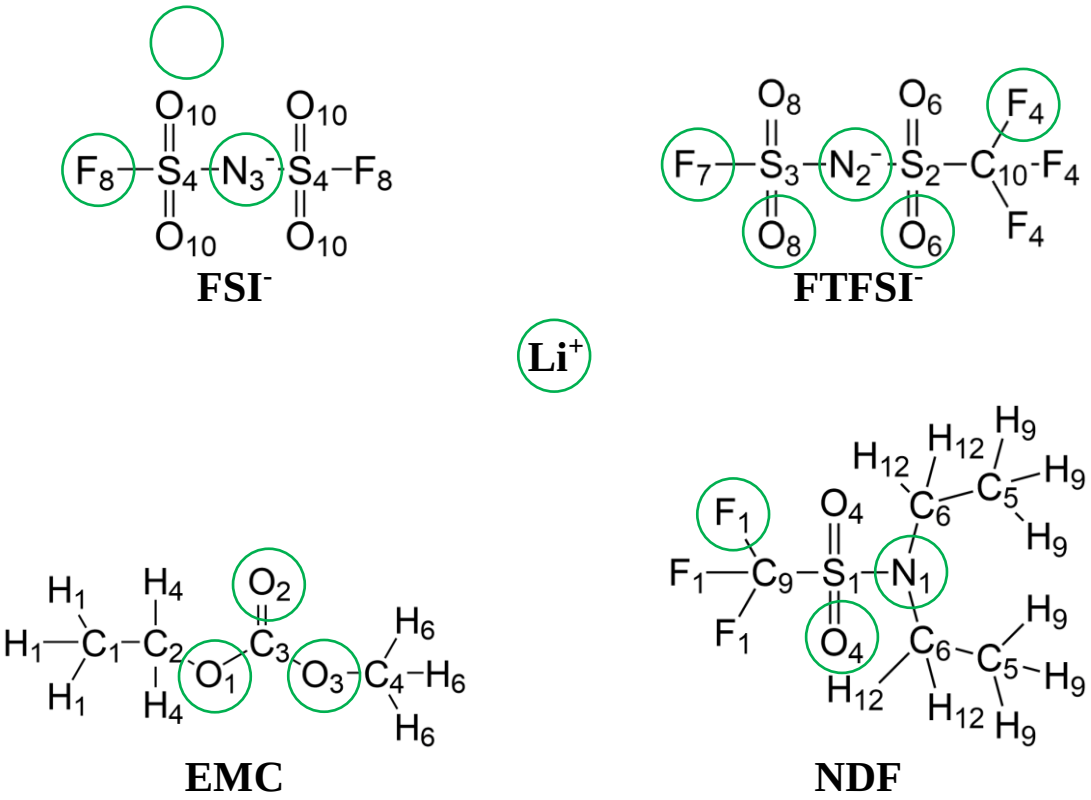

Figure 2.3 Chemical structure of the FSI^- and $FTFSI^-$ anions and molecular solvents of EMC and NDF. Green circles show the putative coordination centers of particles for interactions Li^+ – anion / solvent.

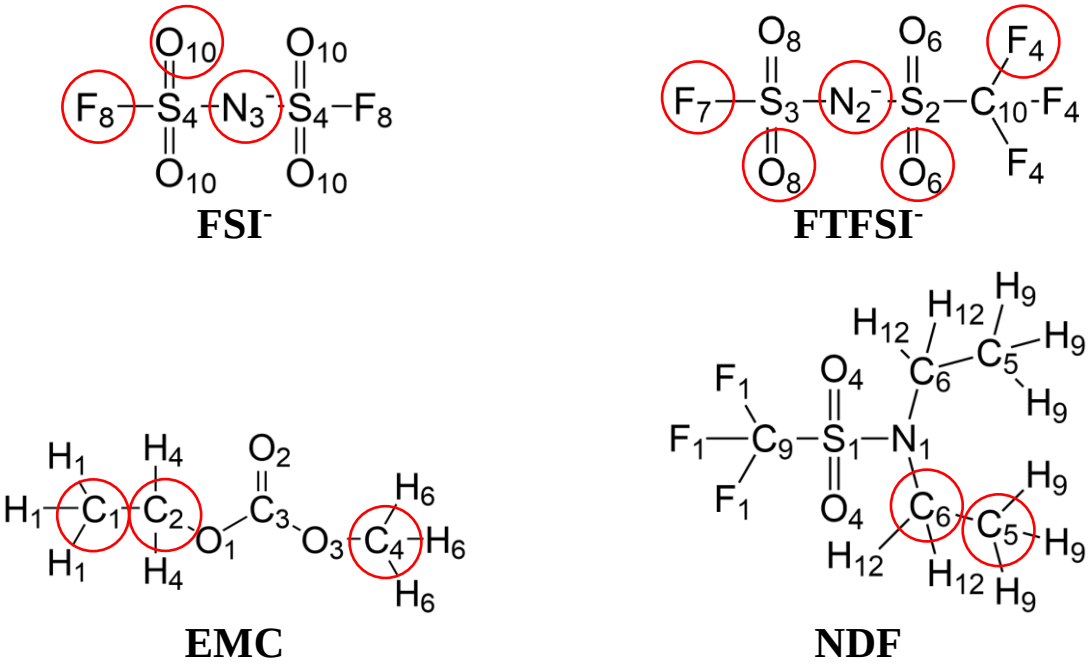

Figure 2.4 Chemical structure of the FSI^- and $FTFSI^-$ anions and molecular solvents of EMC and NDF. Red circles show the putative coordination centers of particles for interactions anion – solvent.

2.5 Transport properties calculations

As part of the investigation of transport properties, the translational self-diffusion coefficients of the centers of mass of molecules and ions were calculated using Einstein's equation based on long-time limit mean squared displacement (MSD) (equation 2.6) [87, 89]:

$$D_i = \frac{1}{6}\lim_{t\to\infty}\frac{d}{dt}\left\langle \left| r_i(t) - r_i(0) \right|^2 \right\rangle, \tag{2.6}$$

where $r_i(t)$ is the is the location of the center of mass of the particle and at the time t.

As an alternative approach, diffusion coefficients can be calculated using the Green-Kubo equation (2.7) [87, 89]:

$$D_i = \frac{1}{3}\int_0^\infty \left\langle v_i(t)\cdot v_i(0)\right\rangle dt \tag{2.7}$$

2.6 Free solvation energy calculations

To characterize the energy change during the transfer of a Lithium ion from a vacuum into a solution (lithium salt in a solvent), the thermodynamic integration method was used. At each step, the Bennett acceptance coefficient was calculated for two physical states close to each other. The free energy of solvation was calculated by integrating the ensemble average of the derivative of the Hamiltonian with respect to λ (2.8) [90]:

$$\Delta G_{solv} = \int_0^1 \left\langle \frac{\partial H}{\partial \lambda} \right\rangle_{NVT;\lambda} d\lambda, \tag{2.8}$$

where H s the Hamiltonian of the system parametrized by the coupling variable λ, which controls the strength of non-bonded interactions. For λ=0, the solute is decoupled from the environment (non-interacting), while at λ=1 all Van der Waals and Coulomb interactions are fully active. For MD simulations of solvation energy, we chose nineteen values of the coupling coefficient λ from 0.10 to 1.00 with a step of 0.05 (figure 2.5).

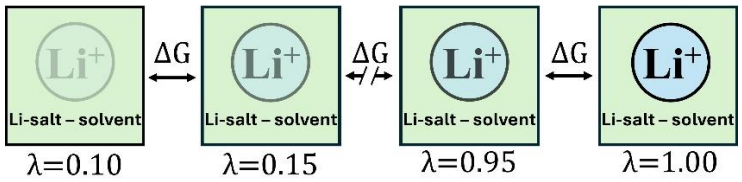

Figure 2.5 Schematic of the thermodynamic integration method used in MD simulation of the free solvation energy

3 RESULTS OF MOLECULAR DYNAMICS SIMULATIONS

3.1 Validation of force fields

Validation of the force fields was carried out by comparing experimental density values with those calculated by molecular dynamics modeling at 298.15 K.

The calculated densities for two models of the force fields are presented in Table 3.1.

Table 3.1 Observed density calculated at 298.15 K for two models of charges in comparison with experimental results.

ρ, kg m^{-3}	**Experimental**	**Model 1** LigParGen (charges of symmetric hydrogen atoms are the arithmetic mean)	**Model 2** LigParGen (charges are recalculated using M062X / AUG-cc-PVTZ / ChelpG)
1. LiFSI-EMC	-	1120.97	1095.48
2. LiFSI-NDF	1401*	1426.69	1402.71
3. LiFTFSI-EMC	-	1135.84	1113.43
4. LiFTFSI-NDF	1414*	1434.87	1412.96
Pure EMC	1006 [91]	1003.47	975.60
Pure NDF	1277 [36]	1335.28	1307.19

* – J. Xu (City University of Hong Kong), private communication.

We chose model 2 because it reproduces the density results for electrolytes better. The choice of this model can also be justified by the fact that the charge on the Nitrogen atom generated by LigParGen is implausibly very negative, more negative than on the Oxygen atom.

3.2 Structure properties

The structure properties of LiFSI and LiFTFSI salts in EMC and NDF solvents at three temperatures were analyzed using radial distribution functions (RDF) and running coordination numbers (RCN).

Figure 3.1 shows the cation-anion RDFs and their corresponding RCNs compared at three different temperatures for LiFSI-EMC system.

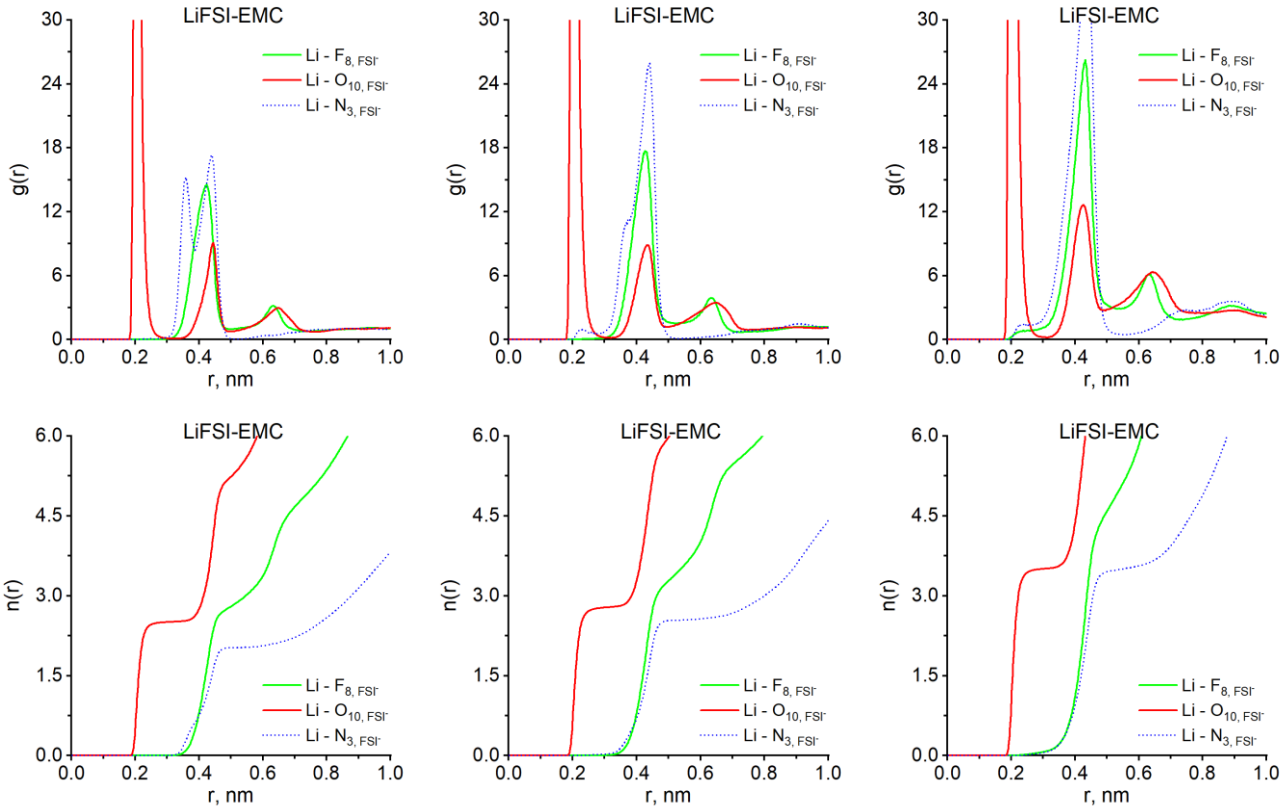

Figure 3.1 Cation – anion RDFs (above) and RCNs (below)
for LiFSI in EMC at: a) 233.15 K; b) 298.15 K; c) 353.15 K.

The first high peak on the RDF plots indicates that the coordination of anions around lithium in the first solvation shell occurs at a distance of 0.20 nm via O_{10} atoms, regardless of temperature. Additionally, the presence of two more maxima (at 0.43 and 0.65 nm, respectively) reveals well-defined second and third solvation shells. The short distance between the cation and the anion within the solvation shells indicates the formation of a contact ion pair, i.e., no solvent molecules are located between the lithium cation and the FSI^- anion. Upon analyzing the peak heights, an increase is observed with rising temperature, indicating a strengthening of the structure. Similarly, the coordination numbers increase and range from 2.51 to 3.51.

The F_8 and N_3 atoms are located at an equal distance from lithium (0.440 nm), corresponding to its second solvation shell. At low temperatures, a distinct double peak is observed (0.358 and 0.440 nm), indicating the approach of a second (neighboring) anion, which is coordinated similarly by nitrogen atoms.

Figure 3.2 shows the cation-solvent RDFs and their corresponding RCNs compared at three different temperatures for LiFSI-EMC system.

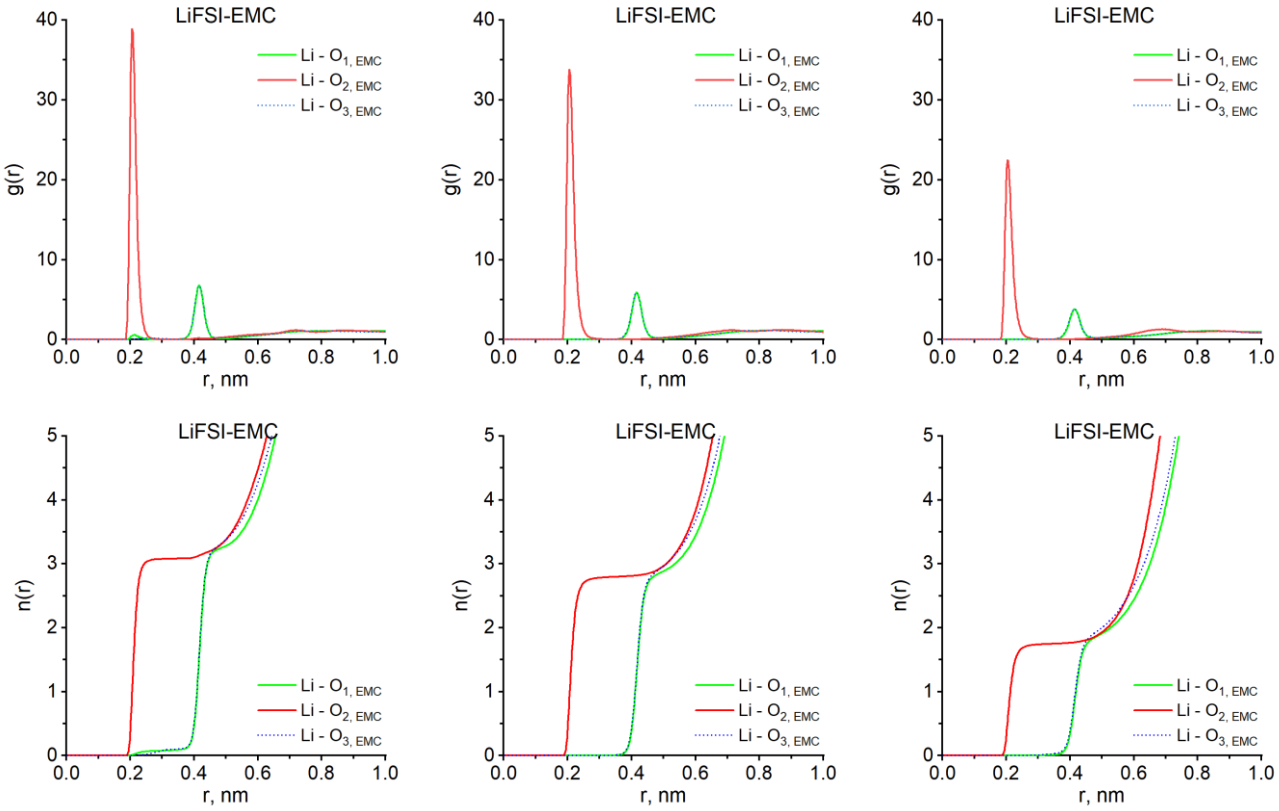

Figure 3.2 Cation – solvent RDFs (above) and RCNs (below)
for LiFSI in EMC at: a) 233.15 K; b) 298.15 K; c) 353.15 K.

Analysis of the RDF curves reveals a distinct structural interaction between the cation and the solvent molecule, which weakens with increasing temperature, although the position of the peaks, similarly to the case of cation–anion interaction, remains unchanged. Nevertheless, at all studied temperatures, the calculated coordination distance remains constant at 0.21 nm, with the solvent coordinating around the lithium cation via O_2 atoms. The coordination number decreases within the range of 3.08 to 1.75.

Figure 3.3 shows the cation-anion RDFs and their corresponding RCNs compared at three different temperatures for LiFSI-NDF system.

Similar to the previous system, the coordination around the lithium cation occurs via O_{10} atoms of the FSI^- anion at a distance of 0.20 nm at all temperatures. Three solvation shells are present; however, the third shell is less pronounced. The coordination numbers at different temperatures are relatively close in value, but the increasing trend is maintained,

ranging from 2.42 to 2.82. Doubling of peaks at the same distances at different temperatures is also observed.

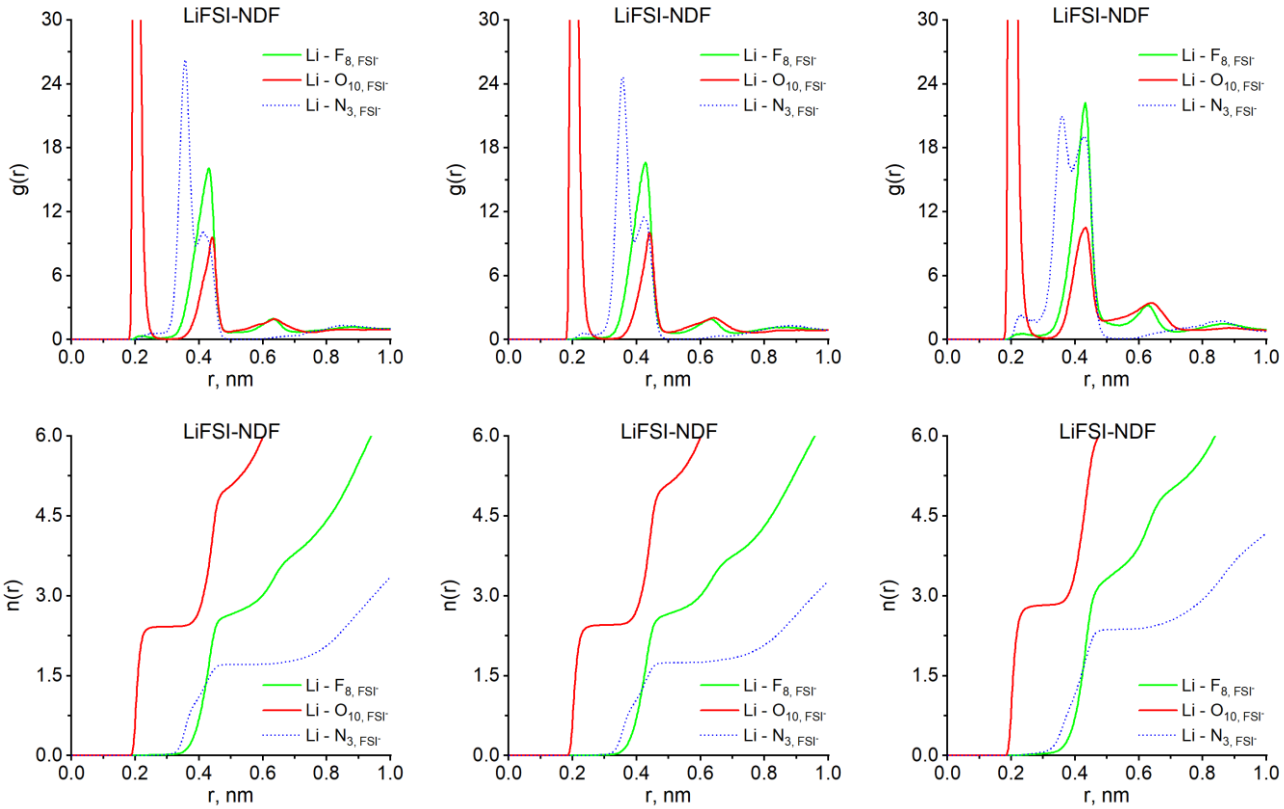

Figure 3.3 Cation – anion RDFs (above) and RCNs (below)
for LiFSI in NDF at: a) 233.15 K; b) 298.15 K; c) 353.15 K.

Figure 3.4 shows the cation-solvent RDFs and their corresponding RCNs compared at three different temperatures for LiFSI-NDF system.

In the case of the system based on the NDF solvent, lithium is coordinated by O_4 atoms at a distance of 0.21 nm. With increasing temperature, the height of the peaks decreases, indicating a decrease in the structuredness of the solvation shell.

Unlike the LiFSI-EMC system, the RDF plots of the LiFSI-NDF show the presence of a second solvation shell, in which O_4 and N_1 atoms are present, with the position of the second maximum at 0.41 – 0.45 nm.

We also observe that there are no structural interactions between lithium and fluorine atoms, as evidenced by the absence of maxima and minima on the RDFs and plateaus on the RCNs.

The coordination numbers in the system with NDF are higher than those in the EMC-based system and decrease with increasing temperature, ranging from 3.17 to 2.64.

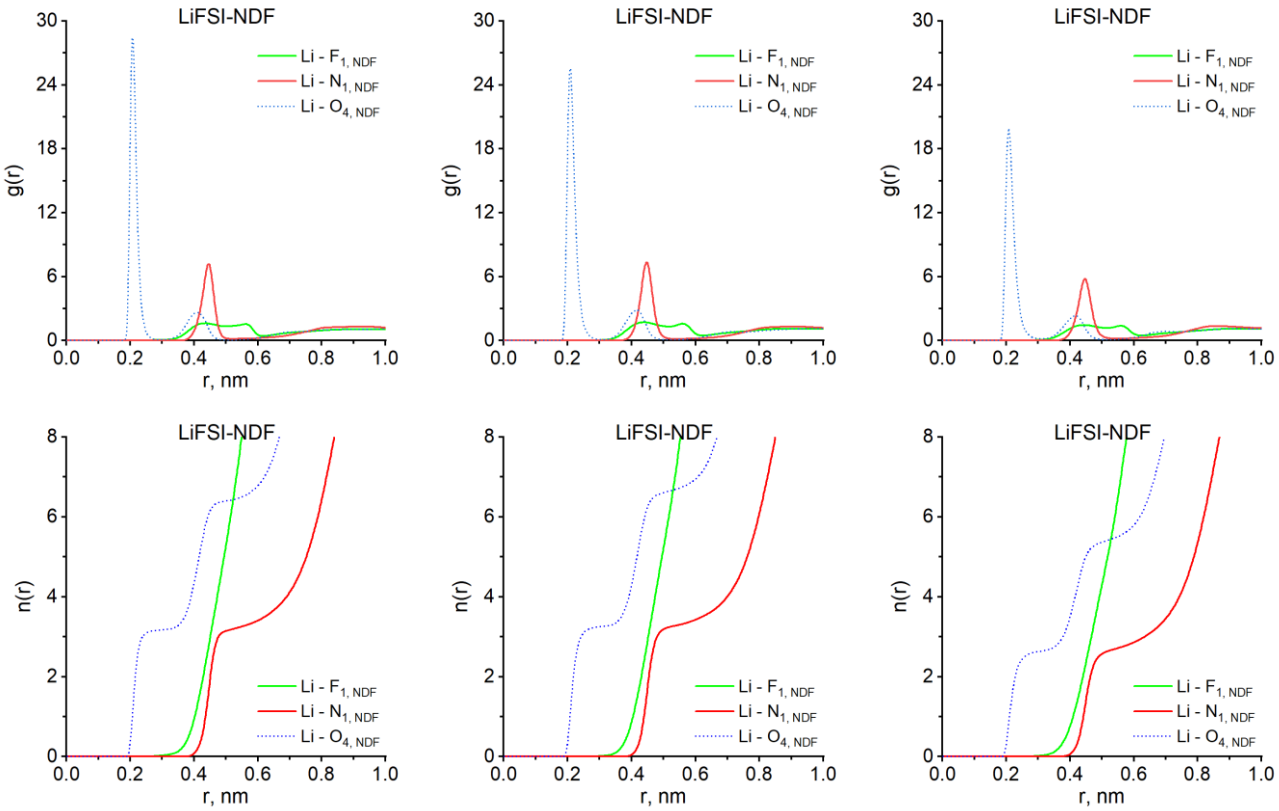

Figure 3.4 Cation – solvent RDFs (above) and RCNs (below)
for LiFSI in NDF at: a) 233.15 K; b) 298.15 K; c) 353.15 K.

Figure 3.5 shows the cation-anion RDFs and their corresponding RCNs compared at three different temperatures for LiFTFSI-EMC system.

As we can see, the coordination of the anion around the lithium cation occurs equally by two oxygen atoms at a distance of 0.20 nm at each temperature. Similarly to the results described above, lithium has three solvation shells. With increasing temperature, the distance from the cation to the O_6 and O_8 atoms shows a slight decreasing trend within 0.022 nm.

A double peak is observed for nitrogen atoms, which are located in the second solvation shell of the lithium cation.

In addition to oxygen and nitrogen, the second solvation shell includes fluorine atoms F_7 (at a distance of 0.43 nm at the studied temperatures).The boundary of the third solvation

shell is 0.64 nm and is characterized by the presence of oxygen and fluorine atoms. No structural interactions between lithium and F_4 are observed.

Overall, with increasing temperature, the interaction intensity also increases, although the distances between atoms change only slightly. The coordination numbers of lithium by oxygen atoms increase with rising temperature in the range from 1.10 to 1.78.

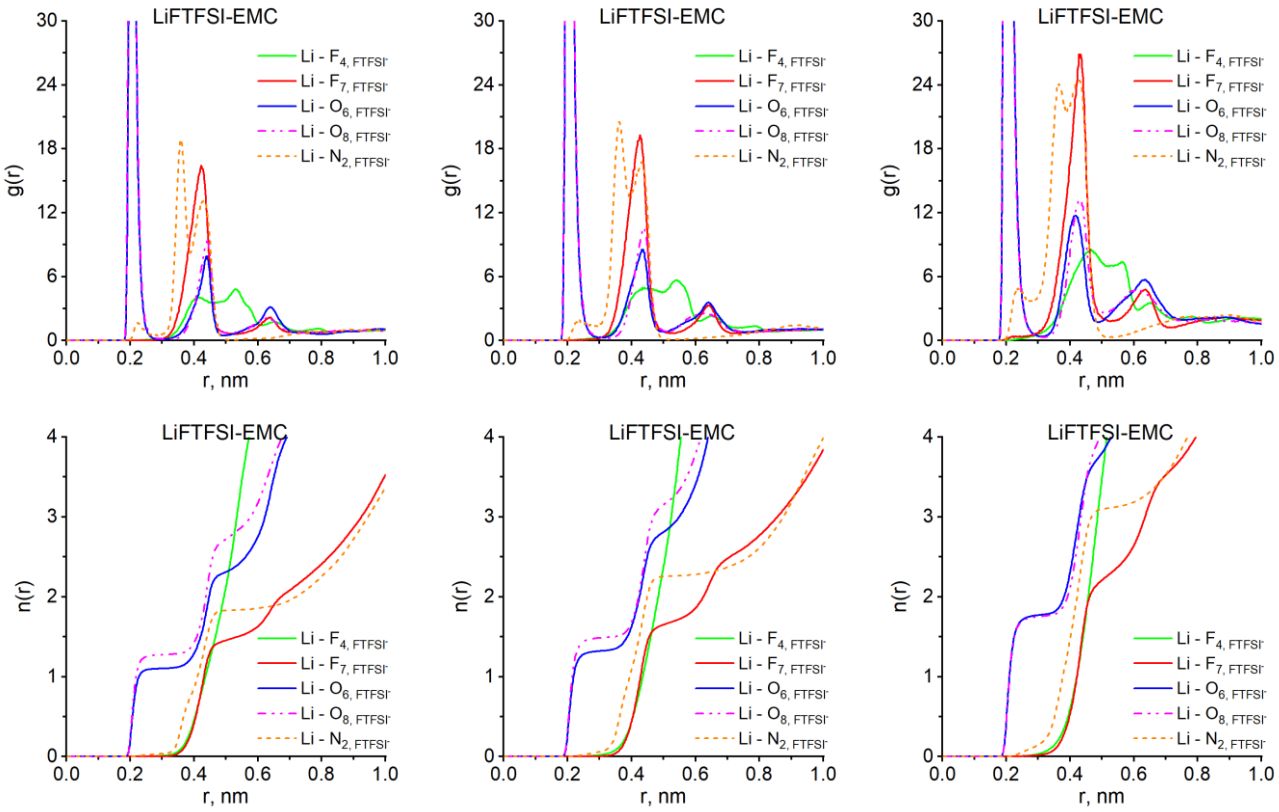

a) b) c)

Figure 3.5 Cation – anion RDFs (above) and RCNs (below)
for LiFTFSI in EMC at: a) 233.15 K; b) 298.15 K; c) 353.15 K.

Figure 3.6 shows the cation-solvent RDFs and their corresponding RCNs compared at three different temperatures for LiFTFSI-EMC system.

According to the results, the structure of this system, when considering the cation-solvent interaction, is similar to LiFSI-EMC. The general trends, appearance, and positions of the maxima and minima on the radial distribution functions, as well as the values of the coordination numbers, completely coincide. Therefore, the change of salt in the system with this solvent did not affect the microstructure.

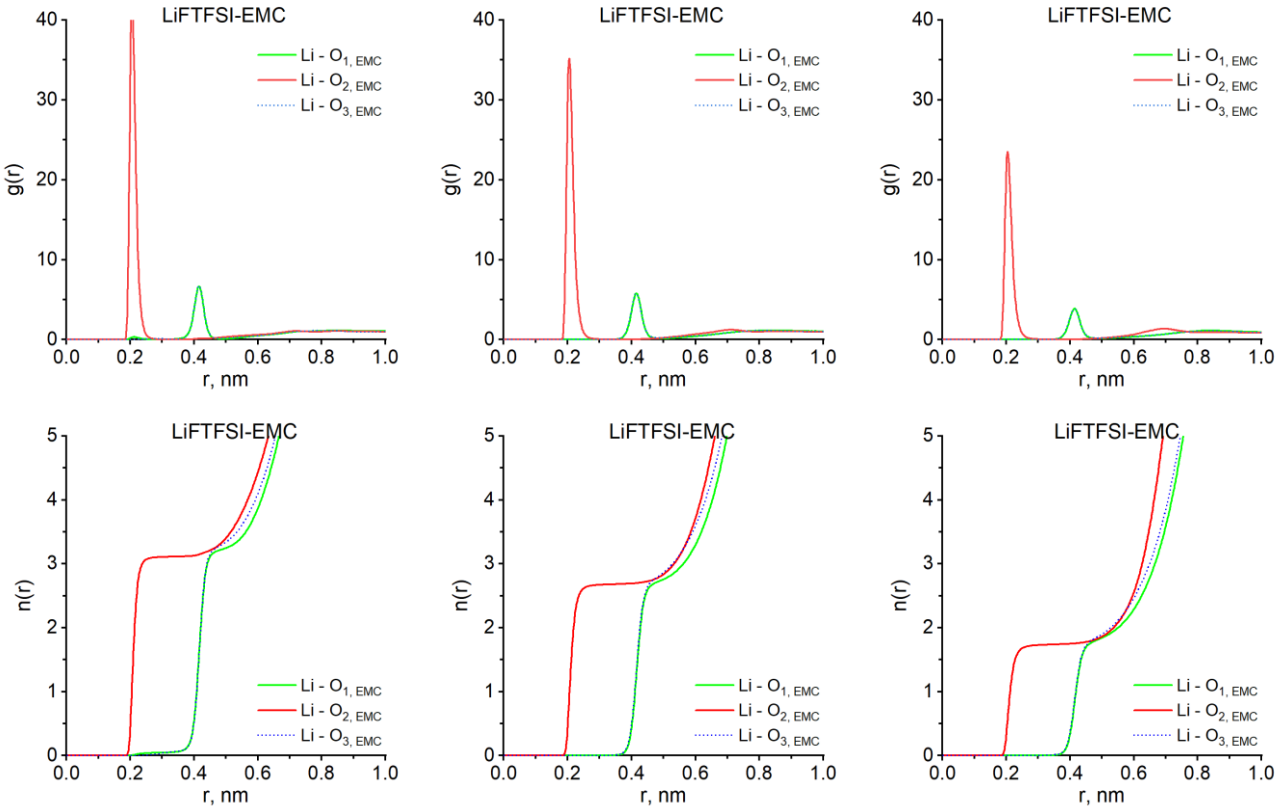

Figure 3.6 Cation – solvent RDFs (above) and RCNs (below)
for LiFTFSI in EMC at: a) 233.15 K; b) 298.15 K; c) 353.15 K.

Figure 3.7 shows the cation-anion RDFs and their corresponding RCNs compared at three different temperatures for LiFTFSI-NDF system.

According to the results, we observe that the change of solvent generally did not affect the nature of the structural interaction lithium-anion and the quantitative indicators. Therefore, the positions of the maxima and their heights coincide with the results for the LiFTFSI-EMC system, the distances between them are similarly small, and thus contact ion pairs are formed in the system. However, in the LiFTFSI-NDF system the third solvation shell is less pronounced.

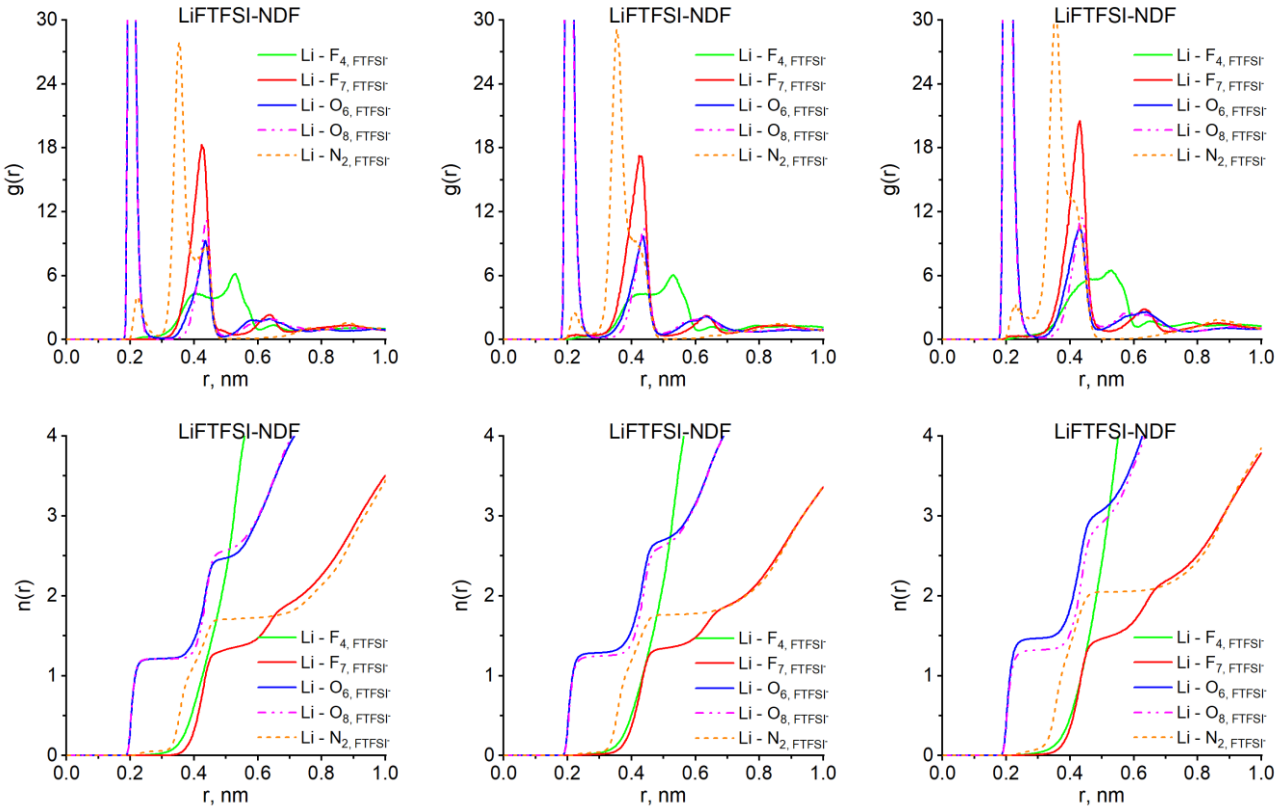

Figure 3.7 Cation – anion RDFs (above) and RCNs (below)
for LiFTFSI in NDF at: a) 233.15 K; b) 298.15 K; c) 353.15 K.

Figure 3.8 shows the cation-solvent RDFs and their corresponding RCNs compared at three different temperatures for LiFTFSI-NDF system.

When comparing two different lithium salts dissolved in NDF, no differences in the cation-solvent interaction were observed.

Comparing the coordination numbers of lithium in the first solvation shell for all four studied systems revealed that, in the case of lithium-anion interactions, the coordination numbers are higher for systems based on the EMC solvent. For lithium-solvent interactions, the coordination numbers are higher for salts with $FTFSI^-$ anion.

The interaction between anions and solvent molecules was investigated for four electrolyte systems at a temperature of 298.15 K. Based on the analysis of RDFs, the absence of characteristic maxima was established, which indicates the absence of specific structural ordering between the anion and the solvent. Additionally, the absence of a plateau on the RCN curves confirms the absence of a stable solvation shell between the anion and

the solvent. The corresponding RDFs and RCNs for the LiFSI-EMC, LiFSI-NDF, LiFTFSI-EMC and LiFTFSI-NDF systems are given in Appendix D.

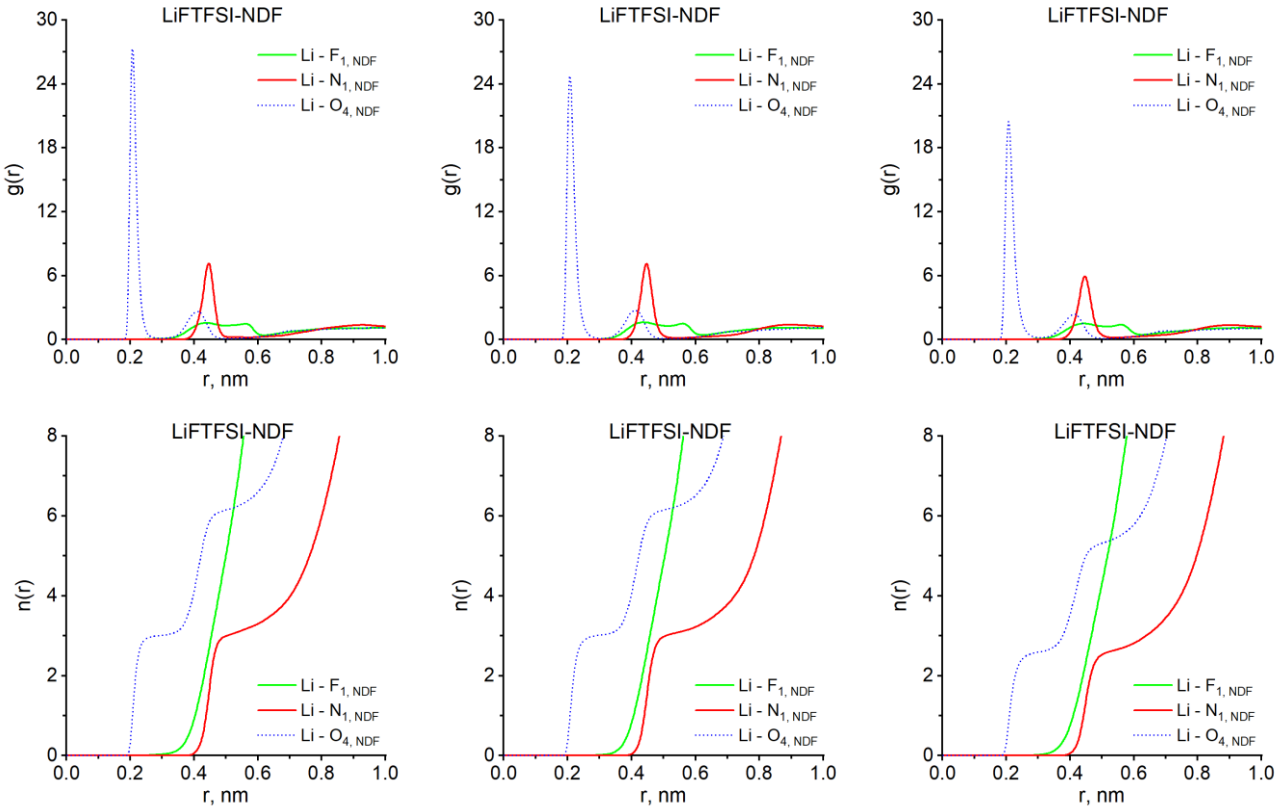

Figure 3.8 Cation – solvent RDFs (above) and RCNs (below) for LiFTFSI in NDF at: a) 233.15 K; b) 298.15 K; c) 353.15 K.

Positions of maxima and minima on radial distribution functions and coordination numbers (CN) of the studied electrolytes at different temperatures are given in Appendix E.

3.3 Transport properties

The transport properties were investigated in terms of diffusion coefficients calculated from the mean squared displacement (MSD) of the center of mass for solvent molecules, the lithium cation, and the anions.

For each mean squared displacement (MSD) curve presented in Appendix F, the diffusion coefficients were calculated from the linear region of the graph.

The diffusion coefficients are presented in Tables 3.2 – 3.3.

Table 3.2 The diffusion coefficients (in 10^{-7} cm^2 s^{-1}) for the solvent molecules, cations and anions from the slope of MSDs for studied electrolytes at different temperatures

D 10^{-7} cm^2 s^{-1}	**233.15 K**	**298.15 K**	**353.15 K**
EMC_{pure}	22.12 ± 0.9	149.15 ± 1.7	341.93 ± 14.9
$EMC_{LiFSI-EMC}$	2.08 ± 0.1	55.29 ± 3.5	199.49 ± 4.1
$EMC_{LiFTFSI-EMC}$	2.71 ± 0.1	58.53 ± 3.7	192.69 ± 5.6
NDF_{pure}	0.74 ± 0.04	22.99 ± 0.3	81.35 ± 2.3
$NDF_{LiFSI-NDF}$	0.029 ± 0.006	1.94 ± 0.2	27.55 ± 3.1
$NDF_{LiFTFSI-NDF}$	0.083 ± 0.025	2.28 ± 0.2	23.89 ± 1.1

Table 3.3 The diffusion coefficients (in 10^{-9} cm^2 s^{-1}) for the solvent molecules, cations and anions from the slope of MSDs for studied electrolytes at different temperatures

D 10^{-9} cm^2 s^{-1}	**233.15 K**	**298.15 K**	**353.15 K**
		LiFSI-EMC	
Li^+	6.56 ± 1.1	76.48 ± 45.9	413.11 ± 622.9
FSI^-	7.10 ± 1.0	76.93 ± 46.2	412.93 ± 621.4
		LiFSI-NDF	
Li^+	0.29 ± 0.1	23.86 ± 4.4	283.11 ± 46.2
FSI^-	0.81 ± 0.3	29.72 ± 5.4	285.55 ± 47.3
		LiFTFSI-EMC	
Li^+	11.45 ± 3.5	80.69 ± 50.5	632.50 ± 358.8
$FTFSI^-$	14.83 ± 3.4	81.25 ± 50.1	647.24 ± 359.2
		LiFTFSI-NDF	
Li^+	0.86 ± 0.4	27.18 ± 5.6	321.06 ± 71.1
$FTFSI^-$	2.02 ± 0.6	31.27 ± 6.9	334.57 ± 76.9

As we can see, in systems based on the EMC solvent, the diffusion coefficients of both the solvent and the ions are higher than those in systems with NDF. In all cases, the anions exhibit greater mobility than the cations, which is consistent with published data [56].

Within systems containing the same solvent, the mobility of both cations and anions is higher in electrolytes with LiFTFSI salt. This can be attributed to the fact that LiFSI salts

tend to form large ionic aggregates, which increase viscosity. This effect is critical for the performance of lithium-ion batteries, as a reduction in the concentration of free charge carriers leads to decreased ionic conductivity [92].

In all studied systems, an increase in temperature leads to greater molecular mobility.

Figure 3.9 shows the temperature dependence of diffusion coefficients as lnD – 1/T.

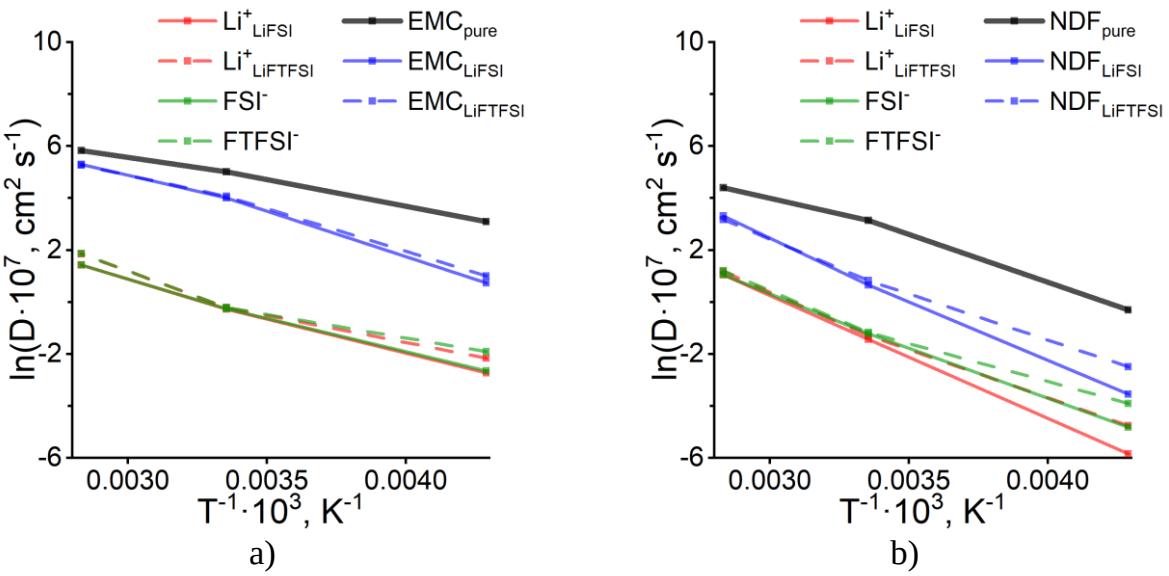

Figure 3.9 Temperature dependence of the diffusion coefficient for systems:

a) based on the EMC solvent; b) based on the NDF solvent.

From this, activation energies were calculated using the Arrhenius equation, the results are presented in Table 3.4.

Table 3.4 Calculated activation energies E_a (kJ mol^{-1}) for solvent molecules and ions

E_a, kJ mol^{-1}	**Solvent**	**Cation**	**Anion**
Pure EMC	15.8	-	-
Pure NDF	27.3	-	-
LiFSI-EMC	26.4	23.4	22.9
LiFSI-NDF	38.9	39.3	33.3
LiFTFSI-EMC	24.7	22.2	20.8
LiFTFSI-NDF	32.0	33.4	28.6

3.4 Lithium free solvation energy

The results of lithium solvation free energy calculations at 298.15 K are presented in Table 3.5.

As expected, for systems with lower lithium diffusion coefficients, its solvation energy exhibits more negative values because stronger solvation hinders ion mobility. Thus, NDF-based systems exhibit superior lithium solvation, leading to the formation of a stable solvation shell but accompanied by reduced lithium cation mobility. Additionally, a difference between LiFSI and LiFTFSI salts is observed. Systems containing LiFTFSI show more negative ΔG_{solv} values.

Table 3.5 Calculated lithium free solvation energy ΔG_{solv} (kJ mol^{-1}) at 298.15 K

	ΔG_{solv} (Li^+), kJ mol^{-1}
LiFSI-EMC	-413.8
LiFSI-NDF	-442.7
LiFTFSI-EMC	-425.0
LiFTFSI-NDF	-446.4

CONCLUSIONS

1. Molecular dynamics simulations of 1 M solutions of LiFSI and LiFTFSI in DMC and NDF at temperatures of 233.15, 298.15 and 353.15 K were performed using the basic OPLS-AA force field supplemented with custom atomic charges.

2. Analysis of radial distribution functions and running coordination numbers revealed that the first solvation shell of lithium contains approximately three FSI^- or two $FTFSI^-$ anions and about three solvent molecules. As temperature increases, the coordination number of lithium ions with anions increases, while their coordination with solvent molecules decreases, with interatomic distances between the cation and the nearest electronegative atoms remaining unchanged.

3. The translational self-diffusion coefficients, calculated from mean square displacements, show that solvent molecules exhibit the highest mobility in the systems. In EMC-based electrolytes, diffusion coefficients of both cations and anions are higher compared to those in NDF. The temperature dependence of diffusion follows the Arrhenius equation. The calculated activation energies range from 20.8 to 26.4 kJ/mol for EMC-based electrolytes and from 28.6 to 39.3 kJ/mol for NDF-based systems.

4. The Gibbs free energies of lithium ion solvation confirm the higher stability of the solvation shell in NDF, particularly in the presence of the $FTFSI^-$ counterion.

LITERATURE SOURCES

1. Li, M.; Lu, J.; Chen, Z.; Amine, K. 30 years of lithium-ion batteries. *Advanced Materials* **2018**, *30* (33), 1800561.

2. Jow, T. R.; Xu, K.; Borodin, O.; Ue, M. *Electrolytes for lithium and lithium-ion batteries*; Springer, 2014.

3. Kalhoff, J.; Eshetu, G. G.; Bresser, D.; Passerini, S. Safer electrolytes for lithium-ion batteries: state of the art and perspectives. *ChemSusChem* **2015**, *8* (13), 2154-2175.

4. Xu, K. Nonaqueous liquid electrolytes for lithium-based rechargeable batteries. *Chemical reviews* **2004**, *104* (10), 4303-4418.

5. Peled, E. The electrochemical behavior of alkali and alkaline earth metals in nonaqueous battery systems—the solid electrolyte interphase model. *Journal of The Electrochemical Society* **1979**, *126* (12), 2047.

6. He, M.; Su, C.-C.; Xu, F.; Amine, K.; Cai, M. Complementary electrolyte design for Li metal batteries in electric vehicle applications. *ACS Applied Materials & Interfaces* **2021**, *13* (22), 25879-25889.

7. Jiang, J.; Dahn, J. Effects of solvents and salts on the thermal stability of LiC6. *Electrochimica Acta* **2004**, *49* (26), 4599-4604.

8. Nutakki, J. S. C. Molecular Modelling of Lithium Salts in the Binary Mixtures of Ethylene and Ethyl Methyl Carbonates. University of Illinois at Chicago, 2023.

9. Xu, K. Electrolytes and interphases in Li-ion batteries and beyond. *Chemical reviews* **2014**, *114* (23), 11503-11618.

10. Qin, M.; Zeng, Z.; Cheng, S.; Xie, J. Challenges and strategies of formulating low-temperature electrolytes in lithium-ion batteries. *Interdisciplinary Materials* **2023**, *2* (2), 308-336.

11. Wiemers-Meyer, S.; Jeremias, S.; Winter, M.; Nowak, S. Influence of battery cell components and water on the thermal and chemical stability of LiPF6 based lithium ion battery electrolytes. *Electrochimica acta* **2016**, *222*, 1267-1271.

12. Kawamura, T.; Okada, S.; Yamaki, J.-i. Decomposition reaction of LiPF6-based electrolytes for lithium ion cells. *Journal of power sources* **2006**, *156* (2), 547-554.

13. Yamada, A.; Ko, S.; Obukata, T.; Shimada, T.; Takenaka, N.; Nakayama, M.; Yamada, Y. Electrode potential dominates the reversibility of lithium metal anodes. **2022**.

14. Parimalam, B. S.; Lucht, B. L. Reduction reactions of electrolyte salts for lithium ion batteries: LiPF6, LiBF4, LiDFOB, LiBOB, and LiTFSI. *Journal of The Electrochemical Society* **2018**, *165* (2), A251.

15. Wang, Q.; Sun, J.; Chu, G.; Yao, X.; Chen, C. Effect of LiPF 6 on the thermal behaviors of four organic solvents for lithium ion batteries. *Journal of thermal analysis and calorimetry* **2007**, *89* (1), 245-250.

16. Lux, S.; Terborg, L.; Hachmöller, O.; Placke, T.; Meyer, H.-W.; Passerini, S.; Winter, M.; Nowak, S. LiTFSI stability in water and its possible use in aqueous lithium-ion batteries: pH dependency, electrochemical window and temperature stability. *Journal of The Electrochemical Society* **2013**, *160* (10), A1694.

17. Han, H.-B.; Zhou, S.-S.; Zhang, D.-J.; Feng, S.-W.; Li, L.-F.; Liu, K.; Feng, W.-F.; Nie, J.; Li, H.; Huang, X.-J. Lithium bis (fluorosulfonyl) imide (LiFSI) as conducting salt for nonaqueous liquid electrolytes for lithium-ion batteries: Physicochemical and electrochemical properties. *Journal of Power Sources* **2011**, *196* (7), 3623-3632.

18. Tan, S.; Ji, Y. J.; Zhang, Z. R.; Yang, Y. Recent progress in research on high-voltage electrolytes for lithium-ion batteries. *ChemPhysChem* **2014**, *15* (10), 1956-1969.

19. Chidiac, J.; Timperman, L.; Anouti, M. Salt and Solvent effect on physicochemical properties and species organisation of Lithium fluorosulfonyl imide (FSI and TFSI) based electrolytes for Li-ion battery: Consequence on cyclability of LiNi0. 8Co0. 15Al0. 05 (NCA) cathode. *Journal of the Taiwan Institute of Chemical Engineers* **2021**, *126*, 88-101.

20. Li, Z.; Wang, L.; Huang, X.; He, X. Lithium Bis (Trifluoromethanesulfonyl) Imide (LiTFSI): A Prominent Lithium Salt in Lithium-Ion Battery Electrolytes–Fundamentals, Progress, and Future Perspectives. *Advanced Functional Materials* **2024**, *34* (48), 2408319.

21. Wu, X.; Du, Z. Study of the corrosion behavior of LiFSI based electrolyte for Li-ion cells. *Electrochemistry Communications* **2021**, *129*, 107088.

22. Yang, B.; Li, C.; Zhou, J.; Liu, J.; Zhang, Q. Pyrrolidinium-based ionic liquid electrolyte with organic additive and LiTFSI for high-safety lithium-ion batteries. *Electrochimica acta* **2014**, *148*, 39-45.

23. Blomgren, G. E. Liquid electrolytes for lithium and lithium-ion batteries. *Journal of Power Sources* **2003**, *119*, 326-329.

24. Ponrouch, A.; Monti, D.; Boschin, A.; Steen, B.; Johansson, P.; Palacín, M. R. Non-aqueous electrolytes for sodium-ion batteries. *Journal of Materials Chemistry A* **2015**, *3* (1), 22-42.

25. Hall, D. S.; Self, J.; Dahn, J. Dielectric constants for quantum chemistry and Li-ion batteries: solvent blends of ethylene carbonate and ethyl methyl carbonate. *The Journal of Physical Chemistry C* **2015**, *119* (39), 22322-22330.

26. Sun, Y.; Radke, C. J.; McCloskey, B. D.; Prausnitz, J. M. Wetting behavior of four polar organic solvents containing one of three lithium salts on a lithium-ion-battery separator. *Journal of colloid and interface science* **2018**, *529*, 582-587.

27. Choi, J.; Shim, E.-G.; Scrosati, B.; Kim, D.-W. Mixed electrolytes of organic solvents and ionic liquid for rechargeable lithium-ion batteries. *Bulletin of the Korean Chemical Society* **2010**, *31* (11), 3190-3194.

28. Hu, P.; Chai, J.; Duan, Y.; Liu, Z.; Cui, G.; Chen, L. Progress in nitrile-based polymer electrolytes for high performance lithium batteries. *Journal of Materials Chemistry A* **2016**, *4* (26), 10070-10083.

29. Wang, Z.; He, Z.; Wang, Z.; Yang, J.; Long, K.; Wu, Z.; Zhou, G.; Mei, L.; Chen, L. A nitrile solvent structure induced stable solid electrolyte interphase for wide-temperature lithium-ion batteries. *Chemical Science* **2024**, *15* (34), 13768-13778.

30. Xu, K.; Angell, C. A. Sulfone-based electrolytes for lithium-ion batteries. *Journal of the Electrochemical Society* **2002**, *149* (7), A920.

31. Flamme, B.; Haddad, M.; Phansavath, P.; Ratovelomanana-Vidal, V.; Chagnes, A. Anodic stability of new sulfone-based electrolytes for lithium-ion batteries. *ChemElectroChem* **2018**, *5* (16), 2279-2287.

32. Shao, N.; Sun, X.-G.; Dai, S.; Jiang, D.-e. Electrochemical windows of sulfone-based electrolytes for high-voltage Li-ion batteries. *The Journal of Physical Chemistry B* **2011**, *115* (42), 12120-12125.

33. Feng, J.; Ai, X.; Cao, Y.; Yang, H. Possible use of non-flammable phosphonate ethers as pure electrolyte solvent for lithium batteries. *Journal of power sources* **2008**, *177* (1), 194-198.

34. Takeuchi, T.; Noguchi, S.; Morimoto, H.; Tobishima, S.-i. Carbonate-modified siloxanes as solvents of electrolyte solutions for rechargeable lithium cells. *Journal of Power Sources* **2010**, *195* (2), 580-587.

35. Smart, M.; Ratnakumar, B.; Surampudi, S. Use of organic esters as cosolvents in electrolytes for lithium-ion batteries with improved low temperature performance. *Journal of the Electrochemical Society* **2002**, *149* (4), A361.

36. Fu, S.-T.; Liao, S.-L.; Nie, J.; Zhou, Z.-B. N, N-dialkyl perfluoroalkanesulfonamides: Synthesis, characterization and properties. *Journal of Fluorine Chemistry* **2013**, *147*, 56-64.

37. Goldbeck, G. The economic impact of molecular modelling of chemicals and materials. *Goldbeck Consulting* **2012**.

38. Badar, M. S.; Shamsi, S.; Ahmed, J.; Alam, M. A. Molecular dynamics simulations: concept, methods, and applications. In *Transdisciplinarity*, Springer, 2022; pp 131-151.

39. Wu, X.; Xu, L. Y.; Li, E. M.; Dong, G. Application of molecular dynamics simulation in biomedicine. *Chemical biology & drug design* **2022**, *99* (5), 789-800.

40. Filipe, H. A.; Loura, L. M. Molecular dynamics simulations: advances and applications. *Molecules* **2022**, *27* (7), 2105.

41. Wang, W. Recent advances in atomic molecular dynamics simulation of intrinsically disordered proteins. *Physical Chemistry Chemical Physics* **2021**, *23* (2), 777-784.

42. Chen, Y.; Krämer, A.; Charron, N. E.; Husic, B. E.; Clementi, C.; Noé, F. Machine learning implicit solvation for molecular dynamics. *The Journal of Chemical Physics* **2021**, *155* (8).

43. Ghahremanian, S.; Rashidi, M. M.; Raeisi, K.; Toghraie, D. Molecular dynamics simulation approach for discovering potential inhibitors against SARS-CoV-2: A structural review. *Journal of molecular liquids* **2022**, *354*, 118901.

44. Tan, X.; Chen, M.; Zhang, J.; Li, S.; Zhang, H.; Yang, L.; Sun, T.; Qian, X.; Feng, G. Decoding Electrochemical Processes of Lithium-Ion Batteries by Classical Molecular Dynamics Simulations. *Advanced Energy Materials* **2024**, *14* (22), 2400564.

45. Yamijala, S. S.; Kwon, H.; Guo, J.; Wong, B. M. Stability of calcium ion battery electrolytes: predictions from ab initio molecular dynamics simulations. *ACS Applied Materials & Interfaces* **2021**, *13* (11), 13114-13122.

46. Alzate-Vargas, L.; Blau, S. M.; Spotte-Smith, E. W. C.; Allu, S.; Persson, K. A.; Fattebert, J.-L. Insight into SEI growth in Li-ion batteries using molecular dynamics and accelerated chemical reactions. *The Journal of Physical Chemistry C* **2021**, *125* (34), 18588-18596.

47. Leimkuhler, B. J.; Reich, S.; Skeel, R. D. Integration methods for molecular dynamics. In *Mathematical Approaches to biomolecular structure and dynamics*, Springer, 1996; pp 161-185.

48. González, M. A. Force fields and molecular dynamics simulations. *École thématique de la Société Française de la Neutronique* **2011**, *12*, 169-200.

49. Kumar, G.; Mishra, R. R.; Verma, A. Introduction to molecular dynamics simulations. In *Forcefields for atomistic-scale simulations: materials and applications*, Springer, 2022; pp 1-19.

50. Tee, S. R.; Searles, D. J. Fully periodic, computationally efficient constant potential molecular dynamics simulations of ionic liquid supercapacitors. *The Journal of Chemical Physics* **2022**, *156* (18).

51. Miranda, D.; Gonçalves, R.; Wuttke, S.; Costa, C. M.; Lanceros-Méndez, S. Overview on theoretical simulations of lithium-ion batteries and their application to battery separators. *Advanced Energy Materials* **2023**, *13* (13), 2203874.

52. Ke, Q.; Gong, X.; Liao, S.; Duan, C.; Li, L. Effects of thermostats/barostats on physical properties of liquids by molecular dynamics simulations. *Journal of Molecular Liquids* **2022**, *365*, 120116.

53. Sun, Z.; Kalhor, P.; Xu, Y.; Liu, J. Extensive numerical tests of leapfrog integrator in middle thermostat scheme in molecular simulations. *Chinese Journal of Chemical Physics* **2021**, *34* (6), 932-948.

54. Frenkel, D.; Smit, B. *Understanding molecular simulation: from algorithms to applications*; Elsevier, 2023.

55. Allen, M. P.; Tildesley, D. J. *Computer simulation of liquids*; Oxford university press, 2017.

56. Da Silva, D. A.; Messias, A.; Fileti, E. E.; Pascon, A.; Franco, D. V.; Da Silva, L. M.; Zanin, H. G. Effect of conductivity, viscosity, and density of water-in-salt electrolytes on the electrochemical behavior of supercapacitors: molecular dynamics simulations and in situ characterization studies. *Materials Advances* **2022**, *3* (1), 611-623.

57. Zhang, Y.; Lewis, N. H.; Mars, J.; Wan, G.; Weadock, N. J.; Takacs, C. J.; Lukatskaya, M. R.; Steinrück, H.-G.; Toney, M. F.; Tokmakoff, A. Water-in-salt LiTFSI aqueous electrolytes. 1. Liquid structure from combined molecular dynamics simulation and experimental studies. *The Journal of Physical Chemistry B* **2021**, *125* (17), 4501-4513.

58. Shao, Y.; Hellström, M.; Yllö, A.; Mindemark, J.; Hermansson, K.; Behler, J.; Zhang, C. Temperature effects on the ionic conductivity in concentrated alkaline electrolyte solutions. *Physical Chemistry Chemical Physics* **2020**, *22* (19), 10426-10430.

59. Tan, W.; Kimura, K.; Tominaga, Y. Li-Ion Mobility and Solvation Structures in Concentrated Poly (ethylene carbonate) Electrolytes: A Molecular Dynamics Simulation Study. *Batteries* **2025**, *11* (2), 52.

60. Sampaio, A. M.; Pereira, G. F. L.; Salanne, M.; Siqueira, L. J. A. Comparing the performance of sulfonium and phosphonium ionic liquids as electrolytes for supercapacitors by molecular dynamics simulations. *Electrochimica Acta* **2020**, *364*, 137181.

61. Bedrov, D.; Piquemal, J.-P.; Borodin, O.; MacKerell Jr, A. D.; Roux, B.; Schröder, C. Molecular dynamics simulations of ionic liquids and electrolytes using polarizable force fields. *Chemical reviews* **2019**, *119* (13), 7940-7995.

62. Kashefolgheta, S.; Wang, S.; Acree, W. E.; Hünenberger, P. H. Evaluation of nine condensed-phase force fields of the GROMOS, CHARMM, OPLS, AMBER, and OpenFF families against experimental cross-solvation free energies. *Physical Chemistry Chemical Physics* **2021**, *23* (23), 13055-13074.

63. Yue, K.; Doherty, B.; Acevedo, O. Comparison between ab initio molecular dynamics and OPLS-based force fields for ionic liquid solvent organization. *The Journal of Physical Chemistry B* **2022**, *126* (21), 3908-3919.

64. Jorgensen, W. L.; Ghahremanpour, M. M.; Saar, A.; Tirado-Rives, J. OPLS/2020 force field for unsaturated hydrocarbons, alcohols, and ethers. *The Journal of Physical Chemistry B* **2023**, *128* (1), 250-262.

65. Yadav, P.; Lamichhane, T. A Comparative Analysis of Force Fields of Drug-Like Molecules: Omeprazole, Favipiravir and Amoxicillin by using Bonded and Non-Bonded Potential Distributions. *Journal of Nepal Physical Society* **2023**, *9* (1), 58-72.

66. Kurt, B.; Temel, H. Development of AMBER parameters for molecular dynamics simulations of boron compounds containing aromatic structure. *Chemical Physics Letters* **2021**, *775*, 138656.

67. Love, O.; Galindo-Murillo, R.; Zgarbová, M.; Šponer, J. i.; Jurečka, P.; Cheatham III, T. E. Assessing the current state of amber force field modifications for DNA─ 2023 Edition. *Journal of Chemical Theory and Computation* **2023**, *19* (13), 4299-4307.

68. Rabet, S.; Raabe, G. Comparison of the GAFF, OPLSAA and CHARMM27 force field for the reproduction of the thermodynamics properties of furfural, 2-methylfuran, 2, 5-dimethylfuran and 5-hydroxymethylfurfural. *Fluid Phase Equilibria* **2022**, *554*, 113331.

69. Poliak, P.; Bleiziffer, P.; Pultar, F.; Riniker, S.; Oostenbrink, C. A Robust and Versatile QM/MM Interface for Molecular Dynamics in GROMOS. *Journal of Computational Chemistry* **2025**, *46* (5), e70053.

70. Costa, L. F.; Germiniani, L. G. L.; Franco, L. F. M. An analysis of the dipalmitoylphosphatidylcholine bilayer gel phases predicted with molecular dynamics simulations using force fields from the GROMOS family. *Fluid Phase Equilibria* **2024**, *583*, 114115.

71. Blanco-González, A.; Wurl, A.; Mendes Ferreira, T.; Piñeiro, Á.; Garcia-Fandino, R. Simulating Bacterial Membrane Models at the Atomistic Level: A Force Field Comparison. *Journal of Chemical Theory and Computation* **2024**, *20* (18), 8290-8307.

72. Fu, C.-F.; Tian, S. X. A comparative study for molecular dynamics simulations of liquid benzene. *Journal of chemical theory and computation* **2011**, *7* (7), 2240-2252.

73. Goloviznina, K. Development and application of molecular interaction models with explicit polarisation for ionic liquids and eutectic solvents. Université de Lyon, 2021.

74. Prusty, S.; Bruschweiler, R.; Cui, Q. Comparative analysis of Im7 dynamics with polarizable and non-polarizable CHARMM family of force fields. **2025**.

75. Lin, F.-Y. Development of the Drude Polarizable Force Field for Molecular Dynamics Simulation. University of Maryland, Baltimore, 2019.

76. Fedkin, M. V.; Shin, Y. K.; Dasgupta, N.; Yeon, J.; Zhang, W.; Van Duin, D.; Van Duin, A. C.; Mori, K.; Fujiwara, A.; Machida, M. Development of the ReaxFF methodology for electrolyte–water systems. *The Journal of Physical Chemistry A* **2019**, *123* (10), 2125-2141.

77. Olou'ou Guifo, S. p. B.; Mueller, J. E.; van Duin, D.; Talkhoncheh, M. K.; van Duin, A. C.; Henriques, D.; Markus, T. Development and validation of a reaxff reactive force field for modeling silicon–carbon composite anode materials in lithium-ion batteries. *The Journal of Physical Chemistry C* **2023**, *127* (6), 2818-2834.

78. De Angelis, P.; Cappabianca, R.; Fasano, M.; Asinari, P.; Chiavazzo, E. Enhancing ReaxFF for molecular dynamics simulations of lithium-ion batteries: an interactive reparameterization protocol. *Scientific Reports* **2024**, *14* (1), 978.

79. Reddivari, S. Electrode-electrolyte Interface Layers in Lithium Ion Batteries using Reactive Force Field Based Molecular Dynamics. 2016.

80. Xue, L.-Y.; Guo, F.; Wen, Y.-S.; Feng, S.-Q.; Huang, X.-N.; Guo, L.; Li, H.-S.; Cui, S.-X.; Zhang, G.-Q.; Wang, Q.-L. ReaxFF-MPNN machine learning potential: a combination of reactive force field and message passing neural networks. *Physical chemistry chemical physics* **2021**, *23* (35), 19457-19464.

81. Selvaraj, S. C.; Koverga, V.; Ngo, A. T. Exploring Li-Ion transport properties of Li3TiCl6: a machine learning molecular dynamics study. *Journal of the Electrochemical Society* **2024**, *171* (5), 050544.

82. Dodda, L. S.; Cabeza de Vaca, I.; Tirado-Rives, J.; Jorgensen, W. L. LigParGen web server: an automatic OPLS-AA parameter generator for organic ligands. *Nucleic acids research* **2017**, *45* (W1), W331-W336.

83. Frisch, A. gaussian 09W Reference. *Wallingford, USA, 25p* **2009**, *470*.

84. Jorgensen, W. L.; Maxwell, D. S.; Tirado-Rives, J. Development and testing of the OPLS all-atom force field on conformational energetics and properties of organic liquids. *Journal of the american chemical society* **1996**, *118* (45), 11225-11236.

85. Kalugin, O.; Volobuev, M.; Kolesnik, Y. V. MDNAES: the program set for computer modelling of ion-molecular systems by using molecular dynamics method. *Kharkov University Bulletin* **1999**, *454*, 58-79.

86. Abraham, M. J.; Murtola, T.; Schulz, R.; Páll, S.; Smith, J. C.; Hess, B.; Lindahl, E. GROMACS: High performance molecular simulations through multi-level parallelism from laptops to supercomputers. *SoftwareX* **2015**, *1*, 19-25.

87. Haile, J. M. *Molecular dynamics simulation: elementary methods*; John Wiley & Sons, Inc., 1992.

88. Haberlandt, R.; Frietzsche, S.; Peinel, G. Grundlagen und Anwendungen. *Wisbaden: Friedr. Vieweg & Sohn Verlagsgesellschaft mbH* **1995**, *19*.

89. Hansen, J.-P.; McDonald, I. R. *Theory of simple liquids: with applications to soft matter*; Academic press, 2013.

90. Bennett, C. H. Efficient estimation of free energy differences from Monte Carlo data. *Journal of Computational Physics* **1976**, *22* (2), 245-268.

91. Haynes, W. M. *CRC handbook of chemistry and physics*; CRC press, 2016.

92. Berhaut, C. L.; Lemordant, D.; Porion, P.; Timperman, L.; Schmidt, G.; Anouti, M. Ionic association analysis of LiTDI, LiFSI and LiPF 6 in EC/DMC for better Li-ion battery performances. *RSC advances* **2019**, *9* (8), 4599-4608.

APPENDIX A

Charge distribution, q, Lennard-Jones parameters, σ and ε, intramolecular parameters, k_i for EMC and NDF

EMC		NDF	
Charge	**q, e**	**Charge**	**q, e**
C^1	-0.275297	C^5	-0.256126
O^1	-0.518027	N^1	-0.306792
O^2	-0.575323	O^4	-0.450581
O^3	-0.410568	F^1	-0.164210
H^4	-0.002211	C^6	0.189894
C^2	0.365447	S^1	0.793574
C^3	0.961193	C^9	0.470582
C^4	0.063697	H^9	0.077774
H^1	0.076369	H^{12}	0.025562
H^6	0.054731		

Atom	**σ, nm**	**ε, kJ/mol**	**Atom**	**σ, nm**	**ε, kJ/mol**
$C^{1,2,4}$	0.350	0.276144	$C^{5,6,9}$	0.350	0.276144
C^3	0.355	0.292880	O^4	0.296	0.711280
$O^{1,3}$	0.290	0.585760	N^1	0.325	0.711280
O^2	0.296	0.878640	F^1	0.290	0.251040
$H^{1,4,6}$	0.250	0.125520	S^1	0.355	1.046000
			$H^{9,12}$	0.250	0.125520

Bond	**r_0, nm**	**k_r, kJ/(mol·nm²)**	**Bond**	**r_0, nm**	**k_r, kJ/(mol·nm²)**
C^1–C^2	0.1529	224262.4	C^5–C^6	0.1529	224262.4
C^2–O^1	0.1410	267776.0	N^1–C^6	0.1449	282001.6
O^1–C^3	0.1327	179075.2	S^1–N^1	0.1670	363171.2
C^3–O^2	0.1229	476976.0	O^4–S^1	0.1440	585760.0
C^3–O^3	0.1327	179075.2	C^9–S^1	0.1770	284512.0
O^3–C^4	0.1410	267776.0	F^1–C^9	0.1360	307105.6
$C^{1,2,4}$–$H^{1,4,6}$	0.1090	284512.0	$H^{9,12}$–$C^{5,6}$	0.1090	284512.0

Angle	**θ, degr**	**k_θ, kJ/(mol·rad²)**	**Angle**	**θ, degr**	**k_θ, kJ/(mol·rad²)**
C^1–C^2–O^1	109.50	418.400	C^5–C^6–N^1	109.70	669.440
$C^{2,3}$–$O^{1,3}$–$C^{3,4}$	116.90	694.544	C^6–N^1–C^6	118.00	418.400
O^1–C^3–O^2	123.40	694.544	C^6–N^1–S^1	120.00	418.400
O^1–C^3–O^3	118.18	584.923	N^1–S^1–O^4	107.00	1004.160
$C^{2,1}$–$C^{1,2}$–$H^{1,4}$	110.70	313.800	N^1–S^1–C^9	103.00	836.800
$O^{3,1}$–$C^{4,2}$–$H^{6,4}$	109.50	292.880	S^1–C^9–F^1	109.50	418.400
O^2–C^3–O^3	123.40	694.544	$C^{6,5}$–$C^{5,6}$–$H^{9,12}$	110.70	313.800
$H^{1,4,6}$–$C^{1,2,4}$–$H^{1,4,6}$	107.80	276.144	N^1–C^6–H^{12}	109.50	292.880
			$H^{9,12}$–$C^{5,6}$–$H^{9,12}$	107.80	276.144
			O^4–S^1–C^9	108.90	619.232
			F^1–C^9–F^1	109.10	644.336

	$O^4–S^1–O^4$	119.00	870.272

APPENDIX A CONTINUED

Improper	φ_S, degr	k_φ, kJ/mol	n	Tetrahedral	φ_S, degr	k_φ, kJ/mol	N
O^3–C^3–O^1–O^2	180.00	43.932	2	S^1–N^1–C^6–C^6	180.00	10.460	2

Dihedral	c_0, kJ/mol	c_1, kJ/mol	c_2, kJ/mol	c_3, kJ/mol	c_4, kJ/mol	c_5, kJ/mol
EMC						
C^3–O^1–C^2–C^1	-2.197	5.201	0.527	-3.531	0.0	0.0
$C^{4,2}$–$O^{3,1}$–C^3–O^2	21.439	0.0	-21.439	0.0	0.0	0.0
$C^{4,2}$–$O^{3,1}$–C^3–$O^{1,3}$	31.206	-9.768	-21.439	0.0	0.0	0.0
H^4–C^2–C^1–H^1	0.628	1.883	0.0	-2.510	0.0	0.0
H^1–C^1–C^2–O^1	0.979	2.937	0.0	-3.916	0.0	0.0
$H^{6,4}$–$C^{4,2}$–$O^{3,1}$–C^3	0.414	1.243	0.0	-1.657	0.0	0.0
NDF						
C^9–S^1–N^1–C^6	-2.897	11.182	12.410	-20.694	0.0	0.0
C^5–C^6–N^1–C^6	6.872	-9.943	3.071	0.0	0.0	0.0
F^1–C^9–S^1–N^1	0.0	0.0	0.0	0.0	0.0	0.0
F^1–C^9–S^1–O^4	0.0	0.0	0.0	0.0	0.0	0.0
H^{12}–C^6–C^5–H^9	0.628	1.883	0.0	-2.510	0.0	0.0
H^9–C^5–C^6–N^1	0.971	2.912	0.0	-3.883	0.0	0.0
H^{12}–C^6–N^1–C^6	0.0	0.0	0.0	0.0	0.0	0.0
H^{12}–C^6–N^1–S^1	-2.935	-1.914	6.096	-1.247	0.0	0.0
O^4–S^1–N^1–C^6	0.0	0.0	0.0	0.0	0.0	0.0
S^1–N^1–C^6–C^5	-3.431	-3.008	10.598	-4.159	0.0	0.0

APPENDIX B

Charge distribution, q, Lennard-Jones parameters, σ and ε,

intramolecular parameters, k_i for FSI^- and $FTFSI^-$ anions

FSI^-			**$FTFSI^-$**		
Charge	**q, e**		**Charge**	**q, e**	
N^3	-0.640210		C^{10}	0.364407	
S^4	1.199082		F^4	-0.168558	
O^{10}	-0.557267		S^2	1.076012	
F^8	-0.264443		O^6	-0.554893	
			N^2	-0.657754	
			S^3	1.233569	
			O^8	-0.559578	
			F^7	-0.281618	
Atom	**σ, nm**	**ε, kJ/mol**	**Atom**	**σ, nm**	**ε, kJ/mol**
N^3	0.325	0.711280	C^{10}	0.350	0.276144
S^4	0.355	1.046000	$F^{4,7}$	0.290	0.251040
O^{10}	0.296	0.711280	$S^{2,3}$	0.355	1.046000
F^8	0.290	0.251040	$O^{6,8}$	0.296	0.711280
			N^2	0.325	0.711280
Bond	**r_0, nm**	**k_r, kJ/(mol·nm^2)**	**Bond**	**r_0, nm**	**k_r, kJ/(mol·nm^2)**
S^4–N^3	0.167	363171.200	F^4–C^{10}	0.136	307105.600
O^{10}–S^4	0.144	585760.000	S^2–C^{10}	0.177	284512.000
F^8–S^4	0.160	281934.656	$O^{6,8}$–$S^{2,3}$	0.144	585760.000
			N^2–$S^{2,3}$	0.167	363171.200
			F^7–S^3	0.160	281934.656
Angle	**θ, degr**	**k_θ, kJ/(mol·rad^2)**	**Angle**	**θ, degr**	**k_θ, kJ/(mol·rad^2)**
N^3–S^4–O^{10}	107.00	1004.160	F^4–C^{10}–F^4	109.10	644.336
N^3–S^4–F^8	104.36	658.311	F^4–C^{10}–S^2	109.50	418.400
S^4–N^3–S^4	118.33	404.760	C^{10}–S^2–O^6	108.90	619.232
O^{10}–S^4–F^8	104.36	658.311	C^{10}–S^2–N^2	103.00	836.80
O^{10}–S^4–O^{10}	119.00	870.272	S^2–N^2–S^3	118.33	404.760
			N^2–$S^{2,3}$–$O^{6,8}$	107.00	1004.160
			N^2–S^3–F^7	104.36	658.311
			O^8–S^3–F^7	104.36	658.311
			$O^{6,8}$–$S^{2,3}$–$O^{6,8}$	119.00	870.272

Dihedral	**c_0, kJ/mol**	**c_1, kJ/mol**	**c_2, kJ/mol**	**c_3, kJ/mol**	**c_4, kJ/mol**	**c_5, kJ/mol**
			FSI^-			
F^8–S^4–N^3–S^4	0.0	0.0	0.0	0.0	0.0	0.0
O^{10}–S^4–N^3–S^4	0.0	0.0	0.0	0.0	0.0	0.0

APPENDIX B CONTINUED

			FTFSI$^-$			
F^7–S^3–N^2–S^2	0.0	0.0	0.0	0.0	0.0	0.0
N^2–S^2–C^{10}–F^4	0.0	0.0	0.0	0.0	0.0	0.0
O^6–S^2–C^{10}–F^4	0.0	0.0	0.0	0.0	0.0	0.0
O^8–S^3–N^2–S^2	0.0	0.0	0.0	0.0	0.0	0.0
S^3–N^2–S^2–C^{10}	-15.611	0.703	20.506	-5.598	0.0	0.0
S^3–N^2–S^2–O^6	0.0	0.0	0.0	0.0	0.0	0.0

APPENDIX C

Sample of atomtypes.itp file for molecular dynamics simulations in GROMACS

```
;
; GENERATED BY LigParGen Server
; Jorgensen Lab @ Yale University
;
[ atomtypes ]
;      name      numb      mass      charge      ptype      sigma      epsilon
    emc_OE         8      15.9990     0.000        A      2.90000E-01  5.85760E-01
    emc_H          1       1.0080     0.000        A      2.50000E-01  1.25520E-01
    emc_CH         6      12.0110     0.000        A      3.50000E-01  2.76144E-01
    emc_CO         8      12.0110     0.000        A      3.55000E-01  2.92880E-01
    emc_OK         8      15.9990     0.000        A      2.96000E-01  8.78640E-01
[ atomtypes ]
;      name      numb      mass      charge      ptype      sigma      epsilon
    fsi_F          9      18.9984     0.000        A      2.90000E-01  2.51040E-01
;   fsi_H          1       1.0080     0.000        A      0.00000E+00  0.00000E+00
    fsi_O          8      15.9990     0.000        A      2.96000E-01  7.11280E-01
    fsi_S         16      32.0600     0.000        A      3.55000E-01  1.04600E+00
    fsi_N          7      14.0070     0.000        A      3.25000E-01  7.11280E-01
[ atomtypes ]
;      name      numb      mass      charge      ptype      sigma      epsilon
    ftf_O          8      15.9990     0.000        A      2.96000E-01  7.11280E-01
    ftf_F          9      18.9984     0.000        A      2.90000E-01  2.51040E-01
    ftf_C          6      12.0110     0.000        A      3.50000E-01  2.76144E-01
;   ftf_H          1       1.0080     0.000        A      0.00000E+00  0.00000E+00
    ftf_S         16      32.0600     0.000        A      3.55000E-01  1.04600E+00
    ftf_N          7      14.0070     0.000        A      3.25000E-01  7.11280E-01
[ atomtypes ]
;      name      numb      mass      charge      ptype      sigma      epsilon
    ndf_H          1       1.0080     0.000        A      2.50000E-01  1.25520E-01
    ndf_F          9      18.9984     0.000        A      2.90000E-01  2.51040E-01
    ndf_O          8      15.9990     0.000        A      2.96000E-01  7.11280E-01
    ndf_S         16      32.0600     0.000        A      3.55000E-01  1.04600E+00
    ndf_C          6      12.0110     0.000        A      3.50000E-01  2.76144E-01
    ndf_N          7      14.0070     0.000        A      3.25000E-01  7.11280E-01
```

APPENDIX D

The calculated RDFs and RCNs of LiFSI and LiFTFSI in EMC and NDF at 298.15 K

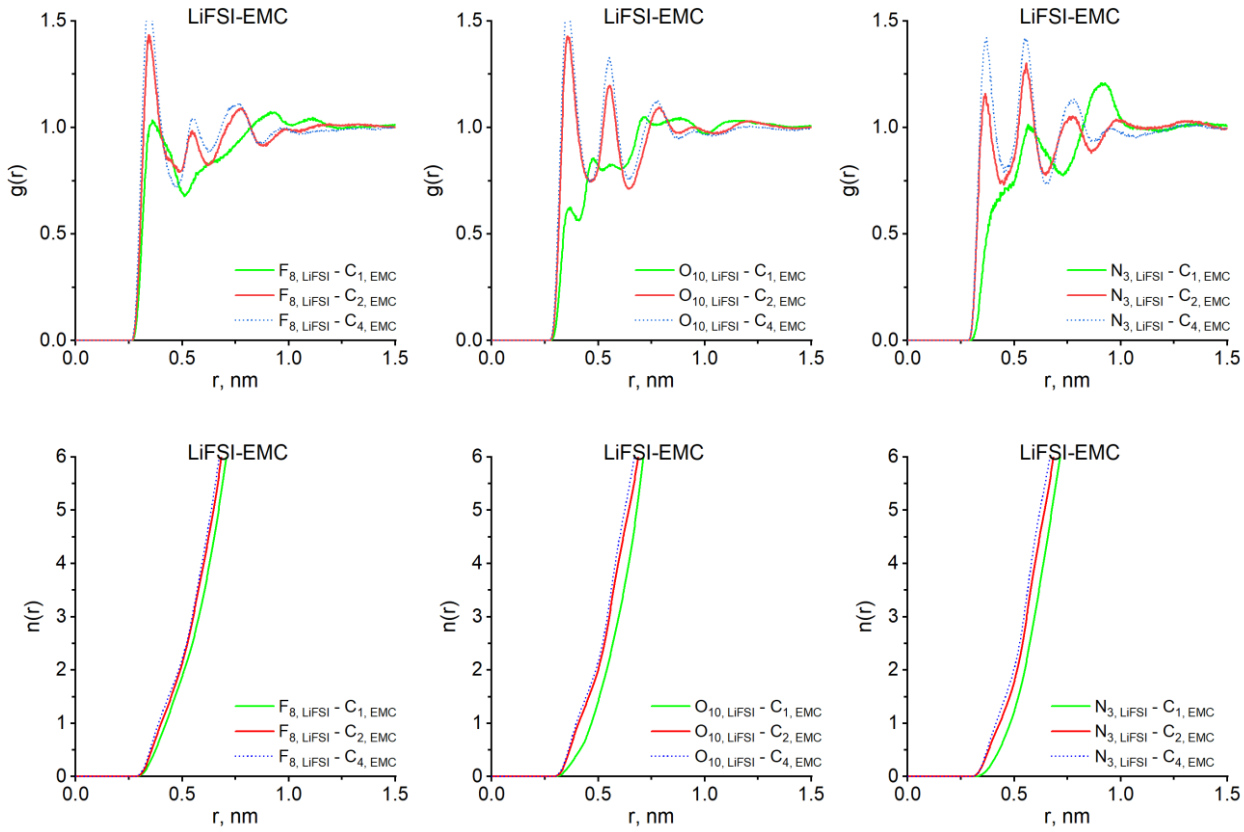

Figure D1 Anion – solvent RDFs (above) and RCNs (below) for LiFSI in EMC at 298.15 K.

APPENDIX D CONTINUED

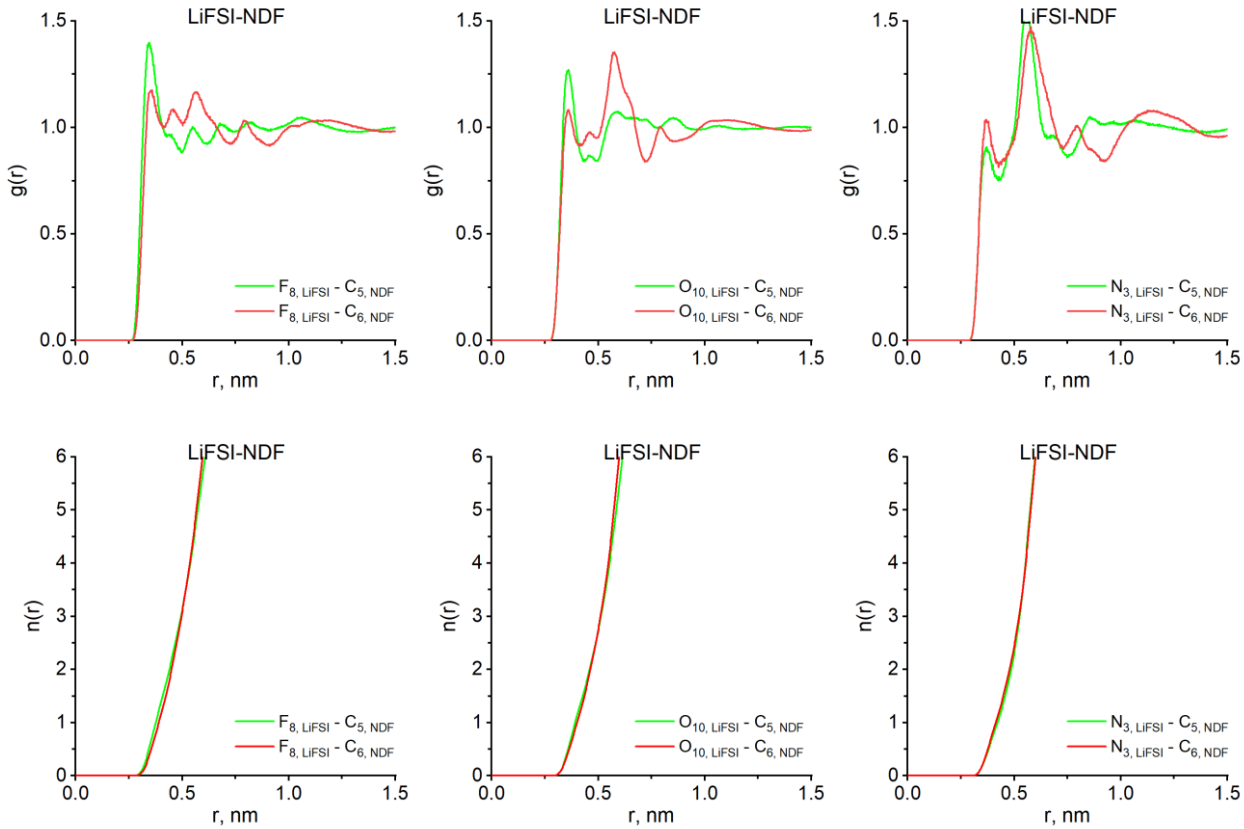

Figure D2 Anion – solvent RDFs (above) and RCNs (below) for LiFSI in NDF at 298.15 K.

APPENDIX D CONTINUED

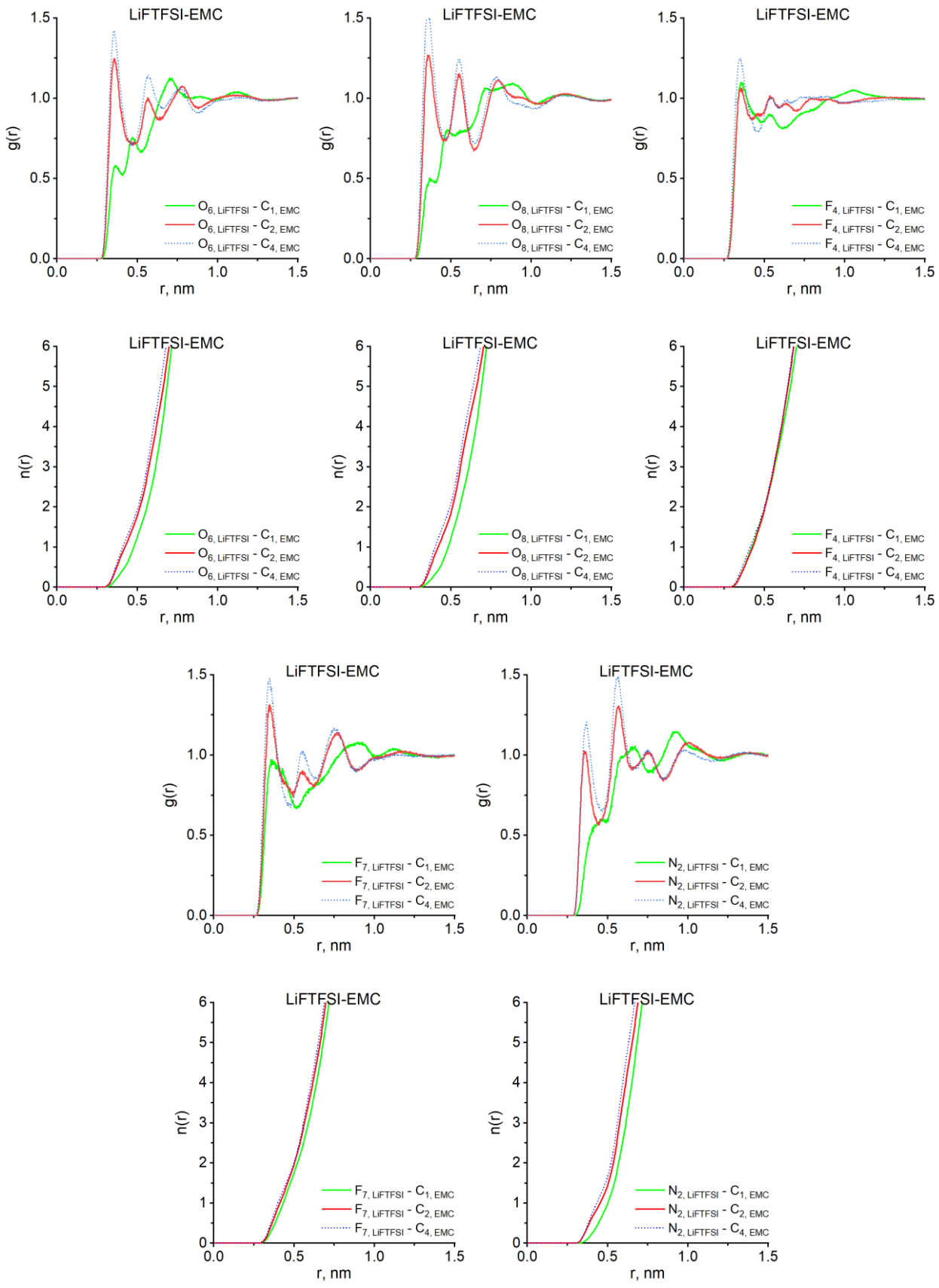

Figure D3 Anion – solvent RDFs (above) and RCNs (below)

for LiFTFSI in EMC at 298.15 K.

APPENDIX D CONTINUED

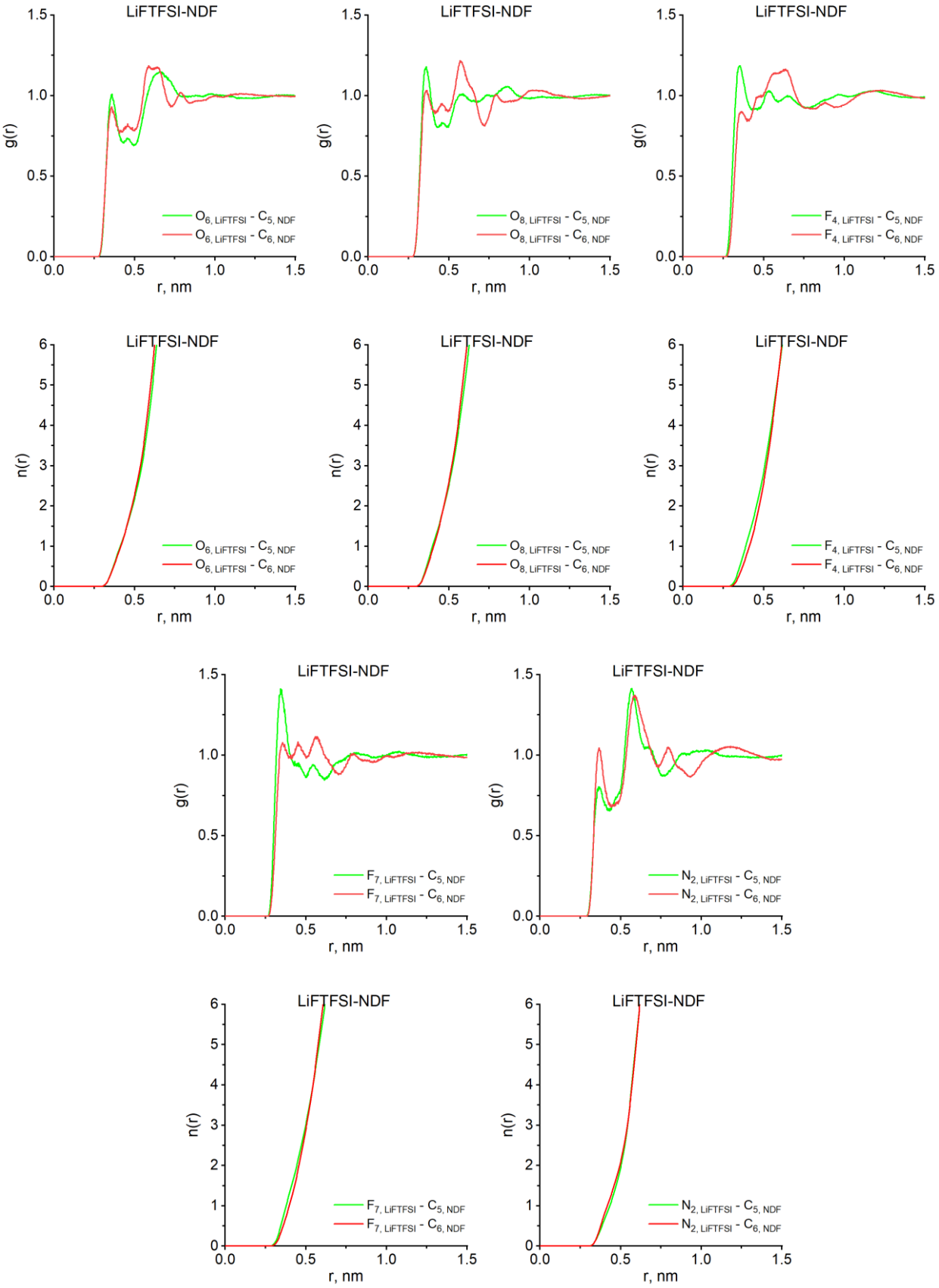

Figure D4 Anion – solvent RDFs (above) and RCNs (below)

for LiFTFSI in NDF at 298.15 K.

APPENDIX E

Positions of maxima and minima on radial distribution functions and coordination numbers (CN) of the studied electrolytes at different temperatures

Table E1 Positions of maxima and minima on RDFs (r, nm) and coordination numbers (CN) of the LiFSI-EMC at different temperatures

233.15 K		**298.15 K**		**353.15 K**	
		Li^+ – anion			
		$Li^+ – F_{8,\ FSI^-}$			
r_{1max}=0.424		r_{1max}=0.426		r_{1max}=0.432	
r_{1min}=0.498	CN=2.79	r_{1min}=0.522	CN=2.88	r_{1min}=0.544	CN=5.05
r_{2max}=0.630		r_{2max}=0.634		r_{2max}=0.636	
r_{2min}=0.732		r_{2min}=0.732		r_{2min}=0.720	
		$Li^+ – O_{10,\ FSI^-}$			
r_{1max}=0.204		r_{1max}=0.202		r_{1max}=0.202	
r_{1min}=0.316	CN=2.51	r_{1min}=0.316	CN=2.51	r_{1min}=0.310	CN=3.51
r_{2max}=0.444		r_{2max}=0.432		r_{2max}=0.426	
r_{2min}=0.508		r_{2min}=0.494		r_{2min}=0.490	
r_{3max}=0.646		r_{3max}=0.648		r_{3max}=0.642	
r_{3min}=0.760		r_{3min}=0.760		r_{3min}=0.768	
		$Li^+ – N_{3,\ FSI^-}$			
r_{1max}=0.358		r_{1max} –		r_{1max} –	
r_{2max}=0.440		r_{2max}=0.440		r_{2max}=0.438	
r_{min}=0.518	CN=2.03	r_{min}=0.534	CN=2.03	r_{min}=0.550	CN=3.50
		Li^+ – solvent			
		$Li^+ – O_{1,\ EMC}$			
r_{max}=0.416		r_{max}=0.416		r_{max}=0.414	
r_{min}=0.482	CN=3.24	r_{min}=0.500	CN=3.28	r_{min}=0.488	CN=1.88
		$Li^+ – O_{2,\ EMC}$			
r_{max}=0.206		r_{max}=0.206		r_{max}=0.204	
r_{min}=0.338	CN=3.08	r_{min}=0.366	CN=3.08	r_{min}=0.340	CN=1.75
		$Li^+ – O_{3,\ EMC}$			
r_{max}=0.416		r_{max}=0.416		r_{max}=0.414	
r_{min}=0.474	CN=3.28	r_{min}=0.496	CN=3.36	r_{min}=0.490	CN=1.96

APPENDIX E CONTINUED

Table E2 Positions of maxima and minima on RDFs (r, nm) and coordination numbers (CN) of the LiFSI-NDF at different temperatures

233.15 K		298.15 K		353.15 K	
Li^+ – anion					
$Li^+ – F_{8,\ FSI^-}$					
r_{1max}=0.430		r_{1max}=0.428		r_{1max}=0.432	
r_{1min}=0.500	CN=2.65	r_{1min}=0.516	CN=2.69	r_{1min}=0.538	CN=3.50
r_{2max}=0.634		r_{2max}=0.634		r_{2max}=0.628	
r_{2min}=0.716		r_{2min}=0.712		r_{2min}=0.726	
$Li^+ – O_{10,\ FSI^-}$					
r_{1max}=0.202		r_{1max}=0.202		r_{1max}=0.200	
r_{1min}=0.308	CN=2.42	r_{1min}=0.306	CN=2.42	r_{1min}=0.312	CN=2.82
r_{2max}=0.442		r_{2max}=0.440		r_{2max}=0.434	
r_{2min}=0.498		r_{2min}=0.504		r_{2min}=0.496	
r_{3max}=0.634		r_{3max}=0.644		r_{3max}=0.640	
r_{3min}=0.744		r_{3min}=0.760		r_{3min}=0.772	
$Li^+ – N_{3,\ FSI^-}$					
r_{1max}=0.352		r_{1max}=0.356		R_{1max}=0.356	
r_{2max}=0.414		r_{2max}=0.422		r_{2max}=0.430	
r_{min}=0.526	CN=1.71	r_{min}=0.514	CN=1.71	r_{min}=0.560	CN=2.38
Li^+ – solvent					
$Li^+ – F_{1,\ NDF}$					
-	-	-	-	-	-
$Li^+ – N_{1,\ NDF}$					
r_{max}=0.446		r_{max}=0.446		r_{max}=0.446	
r_{min}=0.526	CN=3.20	r_{min}=0.538	CN=3.23	r_{min}=0.548	CN=2.71
$Li^+ – O_{4,\ NDF}$					
r_{1max}=0.208		r_{1max}=0.208		r_{1max}=0.208	
r_{2min}=0.298	CN=3.17	r_{2min}=0.308	CN=3.18	r_{2min}=0.312	CN=2.64
r_{2max}=0.412		r_{2max}=0.414		r_{2max}=0.418	
r_{2min}=0.510		r_{2min}=0.514		r_{2min}=0.510	

APPENDIX E CONTINUED

Table E3 Positions of maxima and minima on RDFs (r, nm) and coordination numbers (CN) of the LiFTFSI-EMC at different temperatures

233.15 K		298.15 K		353.15 K	
Li^+ – anion					
$Li^+ – F_{4,\ FTFSI^-}$					
-	-	-	-	-	-
$Li^+ – F_{7,\ FTFSI^-}$					
r_{1max}=0.422		r_{1max}=0.426		r_{1max}=0.428	
r_{1min}=0.536	CN=1.50	r_{1min}=0.532	CN=1.49	r_{1min}=0.528	CN=2.30
r_{2max}=0.640		r_{2max}=0.640		r_{2max}=0.636	
r_{2min}=0.696		r_{2min}=0.722		r_{2min}=0.708	
$Li^+ – O_{6,\ FTFSI^-}$					
r_{1max}=0.204		r_{1max}=0.204		r_{1max}=0.202	
r_{1min}=0.298	CN=1.10	r_{1min}=0.308	CN=1.10	r_{1min}=0.312	CN=1.78
r_{2max}=0.440		r_{2max}=0.432		r_{2max}=0.418	
r_{2min}=0.490		r_{2min}=0.502		r_{2min}=0.486	
r_{3max}=0.638		r_{3max}=0.642		r_{3max}=0.634	
r_{3min}=0.802		r_{3min}=0.760		r_{3min}=0.758	
$Li^+ – O_{8,\ FTFSI^-}$					
r_{1max}=0.204		r_{1max}=0.202		r_{1max}=0.202	
r_{1min}=0.306	CN=1.28	r_{1min}=0.318	CN=1.28	r_{1min}=0.316	CN=1.76
r_{2max}=0.440		r_{2max}=0.438		r_{2max}=0.432	
r_{2min}=0.506		r_{2min}=0.506		r_{2min}=0.510	
r_{3max}=0.634		r_{3max}=0.636		r_{3max}=0.606	
r_{3min}=0.778		r_{3min}=0.782		r_{3min}=0.768	
$Li^+ – N_{2,\ FTFSI^-}$					
r_{1max}=0.358		r_{1max}=0.362		r_{1max}=0.362	
r_{2max}=0.434		r_{2max}=0.432		r_{2max}=0.426	
r_{min}=0.516	CN=1.83	r_{min}=0.524	CN=1.83	r_{min}=0.526	CN=3.11
Li^+ – solvent					
$Li^+ – O_{1,\ EMC}$					
r_{max}=0.416		r_{max}=0.416		r_{max}=0.414	
r_{min}=0.488	CN=3.23	r_{min}=0.490	CN=3.23	r_{min}=0.484	CN=1.81
$Li^+ – O_{2,\ EMC}$					
r_{max}=0.206		r_{max}=0.206		r_{max}=0.204	
r_{min}=0.338	CN=3.11	r_{min}=0.348	CN=3.11	r_{min}=0.344	CN=1.74
$Li^+ – O_{3,\ EMC}$					
r_{max}=0.416		r_{max}=0.414		r_{max}=0.412	
r_{min}=0.478	CN=3.28	r_{min}=0.482	CN=3.29	r_{min}=0.488	CN=1.86

APPENDIX E CONTINUED

Table E4 Positions of maxima and minima on RDFs (r, nm) and coordination numbers (CN) of the LiFTFSI-NDF at different temperatures

233.15 K		298.15 K		353.15 K	
Li^+ – anion					
$Li^+ – F_{4,\ FTFSI^-}$					
-	-	-	-	-	-
$Li^+ – F_{7,\ FTFSI^-}$					
r_{1max}=0.428		r_{1max}=0.430		r_{1max}=0.430	
r_{1min}=0.538	CN=1.64	r_{1min}=0.506	CN=1.33	r_{1min}=0.522	CN=1.49
r_{2max}=0.634		r_{2max}=0.636		r_{2max}=0.632	
r_{2min}=0.700		r_{2min}=0.704		r_{2min}=0.710	
$Li^+ – O_{6,\ FTFSI^-}$					
r_{1max}=0.202		r_{1max}=0.202		r_{1max}=0.200	
r_{1min}=0.308	CN=1.21	r_{1min}=0.286	CN=1.21	r_{1min}=0.308	CN=1.47
r_{2max}=0.436		r_{2max}=0.436		r_{2max}=0.432	
r_{2min}=0.494		r_{2min}=0.502		r_{2min}=0.498	
r_{3max}=0.640		r_{3max}=0.634		r_{3max}=0.638	
r_{3min}=0.754		r_{3min}=0.790		r_{3min}=0.772	
$Li^+ – O_{8,\ FTFSI^-}$					
r_{1max}=0.202		r_{1max}=0.202		r_{1max}=0.200	
r_{1min}=0.316	CN=1.21	r_{1min}=0.300	CN=1.21	r_{1min}=0.308	CN=1.32
r_{2max}=0.438		r_{2max}=0.440		r_{2max}=0.436	
r_{2min}=0.498		r_{2min}=0.500		r_{2min}=0.500	
r_{3max}=0.646		r_{3max}=0.636		r_{3max}=0.634	
r_{3min}=0.770		r_{3min}=0.780		r_{3min}=0.780	
$Li^+ – N_{2,\ FTFSI^-}$					
r_{1max}=0.354		r_{1max}=0.356		r_{1max}=0.356	
r_{2max}=0.434		r_{2max} –		r_{2max} –	
r_{min}=0.496	CN=1.70	r_{min}=0.516	CN=1.71	r_{min}=0.542	CN=2.05
Li^+ – solvent					
$Li^+ – F_{1,\ NDF}$					
-	-	-	-	-	-
$Li^+ – N_{1,\ NDF}$					
r_{max}=0.446		r_{max}=0.446		r_{max}=0.446	
r_{min}=0.526	CN=3.06	r_{min}=0.534	CN=3.09	r_{min}=0.542	CN=2.64
$Li^+ – O_{4,\ NDF}$					
r_{1max}=0.206		r_{1max}=0.208		r_{1max}=0.208	
r_{1min}=0.294	CN=3.01	r_{1min}=0.306	CN=3.02	r_{1min}=0.306	CN=2.60
r_{2max}=0.410		r_{2max}=0.410		r_{2max}=0.416	
r_{2min}=0.500		r_{2min}=0.512		r_{2min}=0.516	

APPENDIX F

The calculated MSDs of solvent molecules, cations and anions in the studied electrolytes at different temperatures

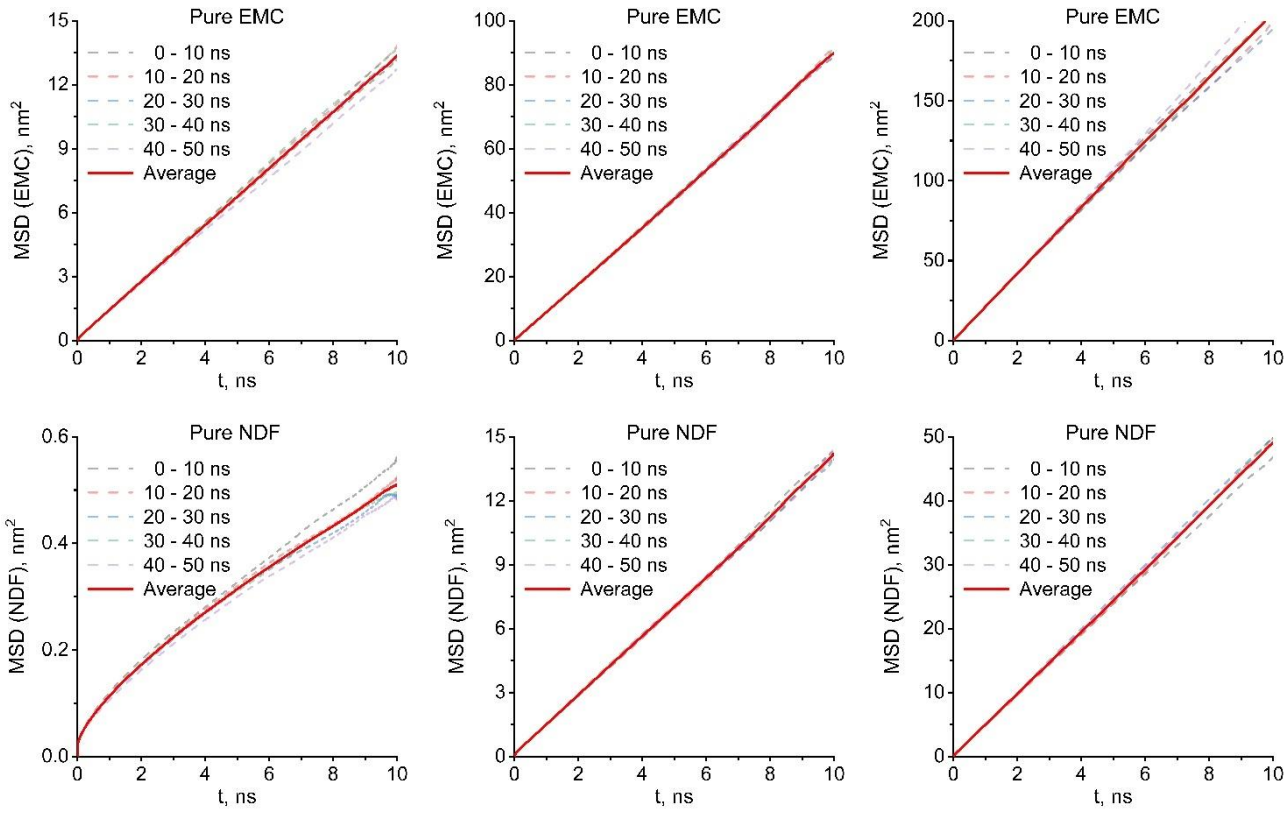

a) b) c)

Figure F1 The calculated MSDs of pure EMC solvent (top) and pure NDF solvent (bottom): a) 233.15 K; b) 298.15 K; c) 353.15K.

APPENDIX F CONTINUED

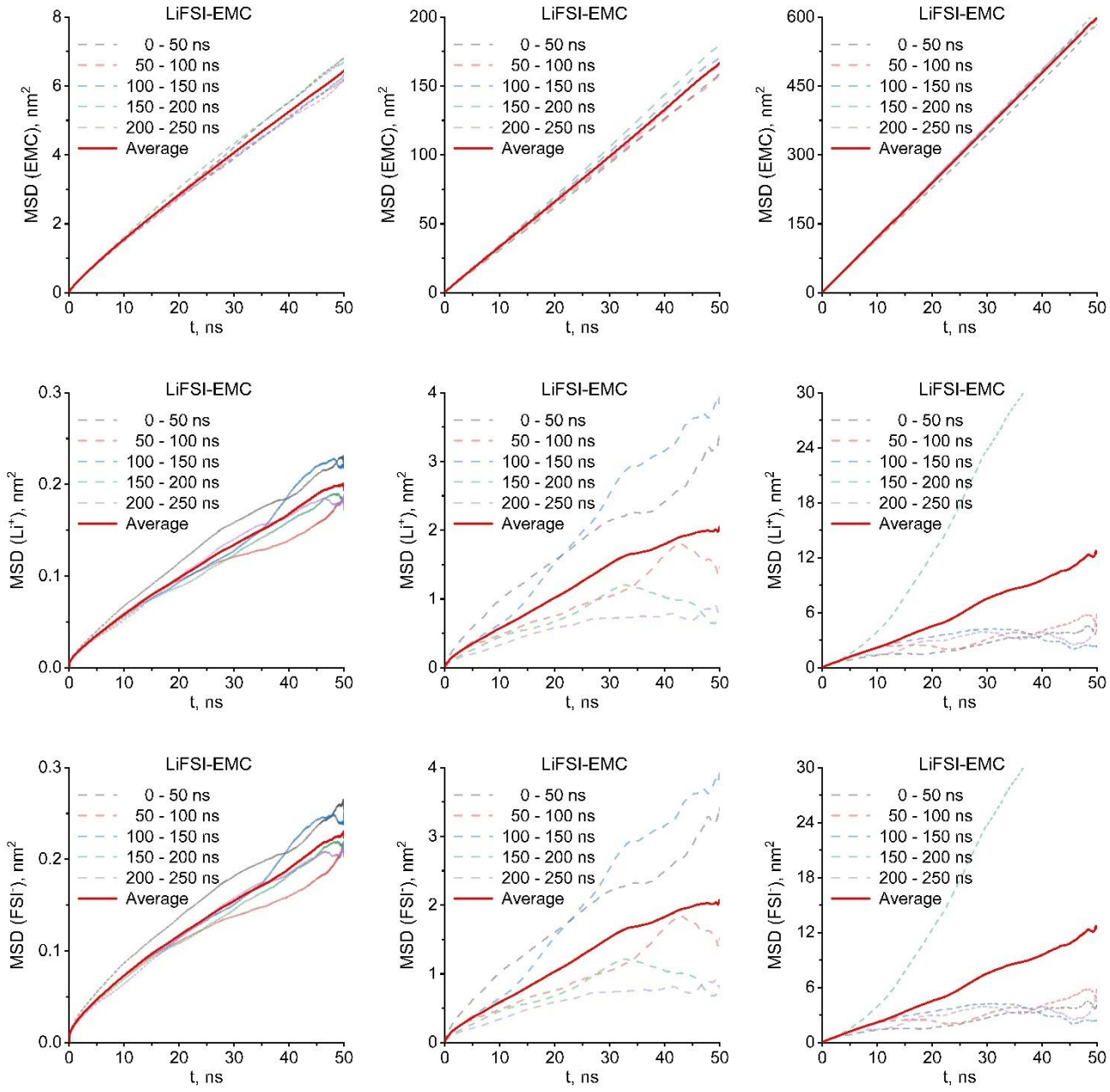

Figure F2 The calculated MSDs of EMC solvent (top), Li^+ cation (middle) and FSI^- anion (bottom) in LiFSI-EMC at: a) 233.15 K; b) 298.15 K; c) 353.15K.

APPENDIX F CONTINUED

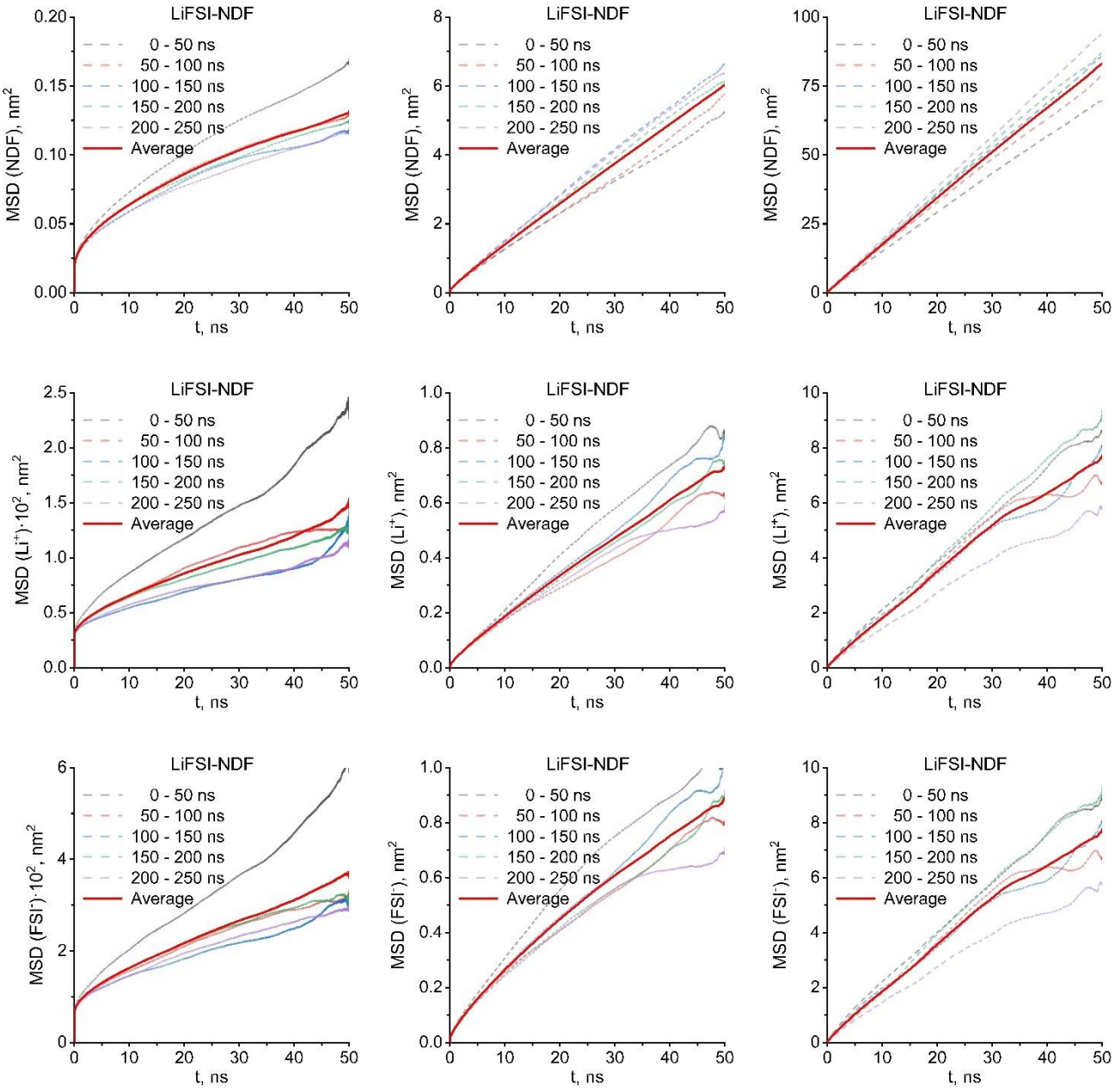

Figure F3 The calculated MSDs of NDF solvent (top), Li^+ cation (middle) and FSI^- anion (bottom) in LiFSI-NDF at: a) 233.15 K; b) 298.15 K; c) 353.15K.

APPENDIX F CONTINUED

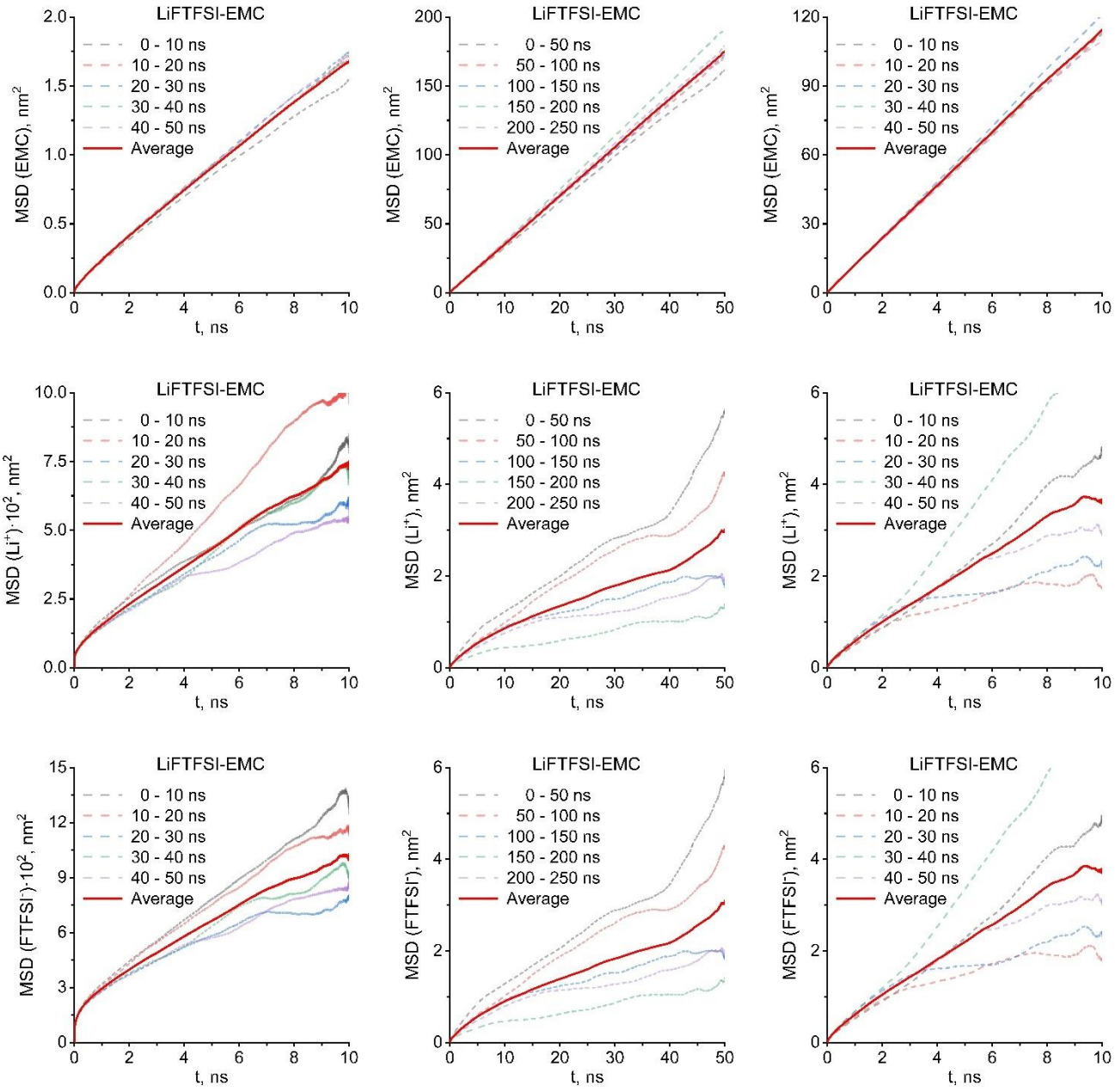

Figure F4 The calculated MSDs of EMC solvent (top), Li^+ cation (middle) and $FTFSI^-$ anion (bottom) in LiFTFSI-EMC at: a) 233.15 K; b) 298.15 K; c) 353.15K.

APPENDIX F CONTINUED

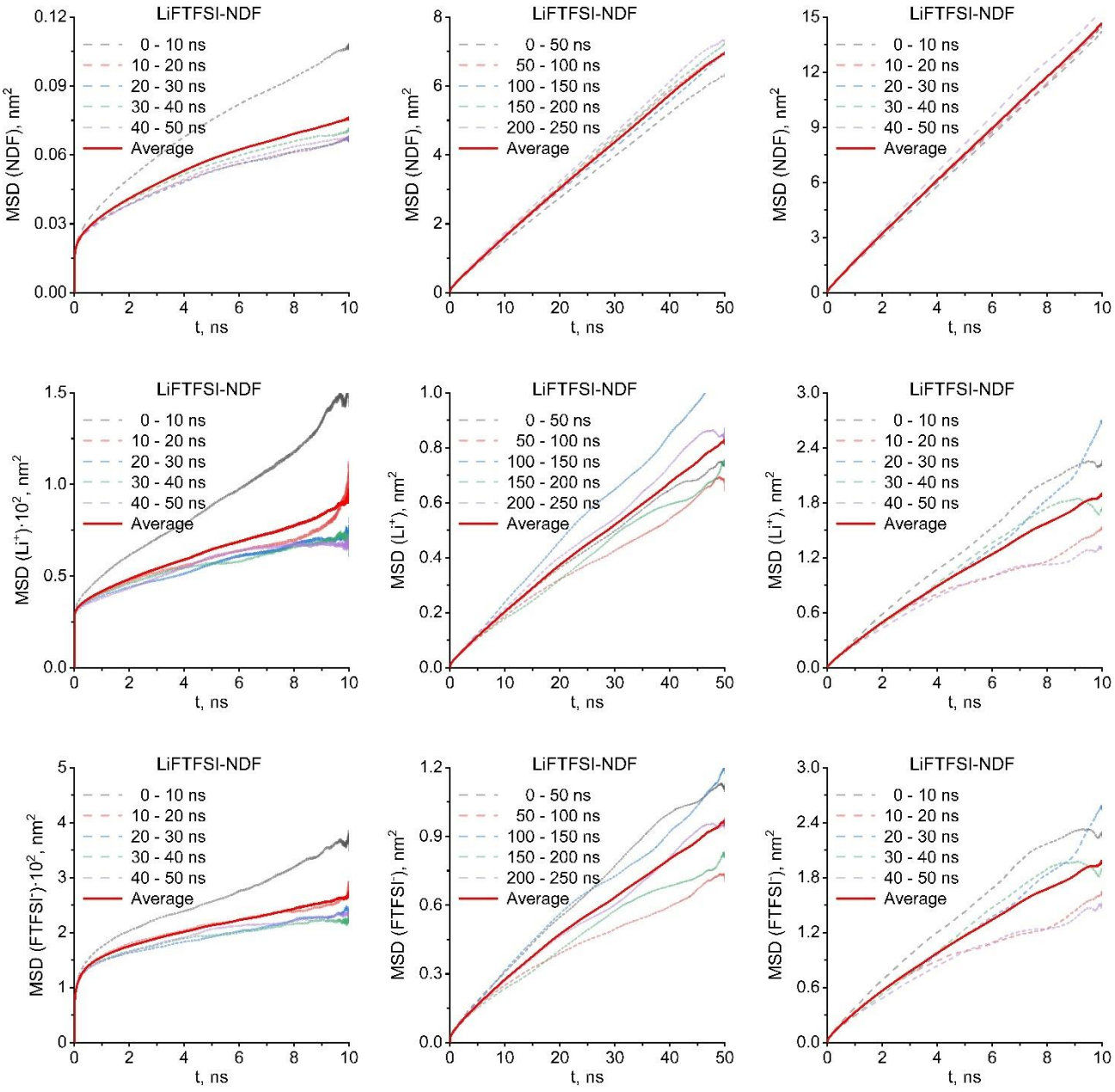

Figure F5 The calculated MSDs of NDF solvent (top), Li^+ cation (middle) and $FTFSI^-$ anion (bottom) in LiFTFSI-NDF at: a) 233.15 K; b) 298.15 K; c) 353.15K.